C. R. Mecanique 347 (2019) 62–89

Contents lists available at ScienceDirect

Comptes Rendus Mecanique

www.sciencedirect.com

Loading rate and confining pressure effect on dilatancy, acoustic emission, and failure characteristics of fissured rock with two pre-existing flaws

Wu Jiangyu [a,b,d,*], Feng Meimei [a,b,*], Han Guansheng [a,b], Yao Benyu [b], Ni Xiaoyan [c]

[a] State Key Laboratory for Geomechanics & Deep Underground Engineering, China University of Mining & Technology, Xuzhou, Jiangsu 221116, China
[b] School of Mechanics & Civil Engineering, China University of Mining & Technology, Xuzhou, Jiangsu 221116, China
[c] School of construction engineering, Jiangsu Vocational Institute of Architectural Technology, Xuzhou, Jiangsu 221116, China
[d] Nottingham Centre for Geomechanics, Faculty of Engineering, University of Nottingham, University Park, Nottingham NG7 2RD, UK

ARTICLE INFO

Article history:
Received 5 July 2018
Accepted 15 October 2018
Available online 6 November 2018

Keywords:
Fissured rock
Pre-existing flaws
Strength
Deformation
Dilatancy
Acoustic emission
Failure

ABSTRACT

Investigating the dilatancy, acoustic emission and failure characteristics of fissured rock are significant to ensure their geotechnical stability. In this paper, the uniaxial and triaxial compression experiments with AE monitoring under different loading rates were carried out on fissured rock specimens with the same geometrical distribution of two pre-existing flaws. The dilatancy and AE activity of these specimens were discussed, and the effects of the confining pressure and loading rate on the mechanical parameters and failure characteristics were analyzed. The results show that the exponential strength criterion is more suitable than the Mohr–Coulomb strength criterion to characterize the strength characteristics of fissured rock. The crack evolution and failure characteristics of fissured rock specimens are more complicated than those of intact rock specimens. The failure characteristics of the fissured rock follow the tensile shear coalescence model, crack branching occurs with increasing the loading rate, and the multi-section coalescence model is verified with increasing the confining pressure. The phenomena of stress drop and yield platform usually occur after the dilatancy onset, the specimen does not fail instantaneously, and the propagation and coalescence of cracks cause a sharp increase in the AE signals, circumferential strain, and volumetric strain.

List of symbols

A	Length of the pre-existing flaw AE acoustic emission
b_1, b_2, b_3	Geometric parameters of the pre-existing fissure
c	Peak point
c	Cohesive force

* Corresponding authors at: State Key Laboratory for Geomechanics & Deep Underground Engineering, China University of Mining & Technology, Xuzhou, Jiangsu 221116, China.
E-mail addresses: wujiangyu@cumt.edu.cn (J. Wu), fengmeimei@cumt.edu.cn (M. Feng).

https://doi.org/10.1016/j.crme.2018.10.002
1631-0721/

cc Initial point of elastic deformation
cd Dilatancy onset
ci Terminal point of elastic deformation
D Region between cd and failure
E_s Elastic modulus
F, f_1, f_2 Strength parameters of the exponential strength criterion
I_i Point of existence of a stress drop
I_1 Initial point of existence of a stress drop
L Length of the rock bridge
M, N Strength parameters of Mohr–Coulomb's strength criterion
N Number of pre-existing flaws
O Initial point of pore compaction
UCS Uniaxial compressive strength
XRD X-ray diffraction
α Angle of the pre-existing flaw
β Angle of the rock bridge
ε_{1c} Axial peak strain
ε_{3c} Circumferential peak strain
ε_{vc} Volumetric peak strain
ε_{1cd} Axial strain of the dilatancy onset
ε_{3cd} Circumferential strain of the dilatancy onset
ε_{vcd} Volumetric strain of the dilatancy onset
σ_{1c} Peak strength (when $\sigma_3 = 0$ MPa, $\sigma_{1c} = \mathrm{UCS}$)
σ_{1cd} Axial stress of the dilatancy onset
φ Internal friction angle

1. Introduction

The engineering rock mass contains some faults such as joints, initial fissures, and weak boundaries in general, and the new cracks easily initiate under disturbance [1–7]. The existence of these defects causes the rock material to present obvious heterogeneity and discontinuity under multiple external loads, which seriously affects the engineering behavior of rock mass [8–10]. For example, in the slope construction of highway, railway, and dam, the weak faults in the bedrock are ceaseless to evolve to form the fracture plane under the impact of pore water and long-term rain erosion, which results in layered deformation and failure in slope [11–15]. In tunneling and mining engineering, the full development of fissures causes damage on geotechnical structure to form the underground watercourse, which results in the inrush of clay and water [16–24]. Therefore, investigating the mechanical behaviors of fissured rock is significant to ensure their geotechnical stability [25,26].

About fissured rock, numerous geotechnical scientists and predecessors carried out lots of experiments and numerical simulations to investigate its mechanical behavior, in which they obtained remarkable achievements and contributions. The main concern is the effect of fissure geometrical distribution on the mechanical behaviors fissured rock, including flaw parameters of number, angle, and length, as well as rock segment bridge parameters of angle and length [27–35]. These authors not only discussed the variation of mechanical parameters, but also revealed the mechanism of crack propagation, and the evolution characteristics of crack were described in detail [36–43]. More in-depth knowledge is needed to understand structure evolution inside fissured rock, such as the observation of its internal structure with computed tomography (CT), the localization of crack damage by acoustic emission (AE), and simulated reproduction using numerical software [44–51]. In addition, some scholars studied the influence of lithology, temperature, chemical corrosion, and stress conditions on its mechanical behavior, due to differences in engineering and geological conditions [52–57].

The above researches mainly focused on the mechanical behavior of rocks under uniaxial compression. However, the rock mass is generally in three-dimensional compression [58–61]. Thus, it is necessary to systematically study the mechanical behavior of fissured rock, especially for its AE, deformation characteristics and crack evolution during dilatancy. And the factors that can affect the mechanical parameters of fissured rock are multiple, in which the diverse external loads cause difficulties in the quantification of strength parameters, thereby resulting in a failure in engineering parameters [62–68]. In this paper, uniaxial and triaxial compression experiments with AE monitoring under different loading rates were carried out on fissured rock specimens with the same geometrical distribution of two pre-existing flaws. The dilatancy and AE activity of these specimens were discussed, and the effects of the confining pressure and loading rate on the mechanical parameters and failure characteristics were analyzed.

Table 1
Main physical properties of red sandstone.

Dry density (g/cm^3)	Natural density (g/cm^3)	Saturated density (g/cm^3)	Porosity	Saturated water content (%)
2.39	2.42	2.45	0.06	2.45

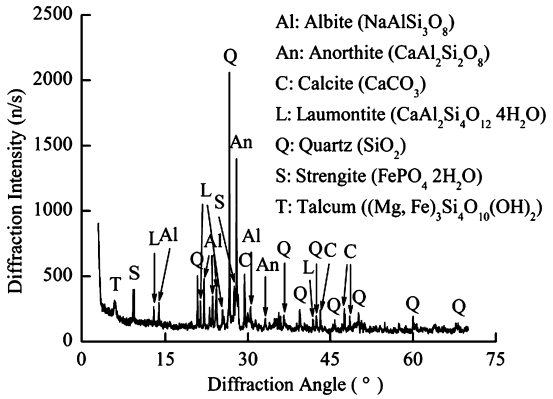

Fig. 1. XRD spectrum of a rock sample.

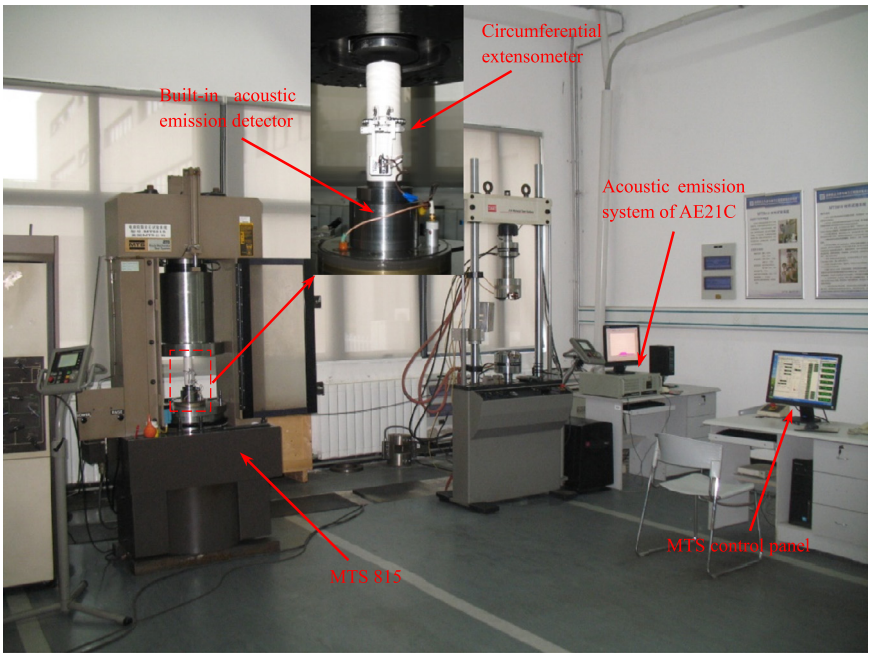

Fig. 2. Experimental system.

2. Experimental methods

2.1. Experimental material

The rock sample was obtained from a mine in Xuzhou, Jiangsu, China. Table 1 shows its main physical properties and Fig. 1 gives its X-ray diffraction (XRD).

2.2. Experimental equipment

Fig. 2 presents the experimental equipment. The MTS815 test system is applied to compress the rock specimen, and the AE monitoring device is the AE21C system. During AE monitoring on rock specimen in triaxial test, the AE detector was usually placed on the hydraulic cylinder. The AE signals need to pass through hydraulic oil and the hydraulic cylinder

Table 2
Main equipment parameters of MTS815.

Device	Loading rates (mm/s)	Fatigue frequency (Hz)	Frame stiffness (N/m)
MTS815	10^{-5}–1	0.001–0.5	10.5×10^9

Table 3
Main equipment parameters of AE21C.

Device	Detector type	Gain and threshold (dB)	Impact time (μs)	Impact interval (μs)	Acquisition rate (ms/time)
AE21C	Piezoelectric ceramic acoustic emission sensor	35	50	300	100

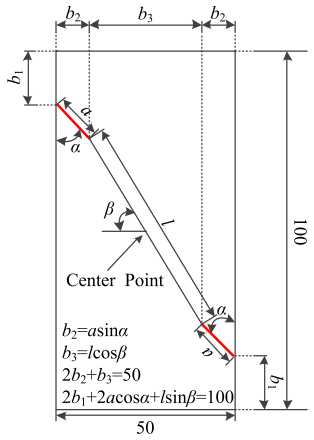

Fig. 3. Flaw distribution of a fissured rock specimen.

during transmission, which inevitably deteriorates its transmission and accuracy. Therefore, the base of the MTS815 has been reformed, the AE detector can be built in the hydraulic cylinder for direct obtaining of AE data, which not only allows us to overcomes the above difficulty, but also greatly improves the accuracy of AE signals. The main equipment parameters are given in Table 2 and Table 3.

2.3. Experimental specimens

The intact rock specimen is a cylinder of Ø 50×100 mm, which is a standard recommended by the International Society for Rock Mechanics (ISRM) [69]. It should be noted that the non-parallelism and non-perpendicularity of the specimen must be controlled in the range of (-0.02 mm, $+0.02$ mm). The fissured rock specimen with two pre-existing flaws is produced on the intact specimen using a cutting machine [70,71]. Fig. 3 presents the flaw distribution. The red segments are the pre-existing flaws, n is their number, a is the length, and α is the angle. The connection between the tips of the two pre-existing flaws is the rock segment bridge, l is its length, and β is the angle. There have been lots of researches to discuss the influence of flaw distribution on the mechanical parameters of fissured rock [72]. However, the mechanical behavior of fissured rock under different external loads is not clear, especially for the characterization of the dilatancy behavior. In addition, the multiple geometric distributions of pre-existing flaws cause huge differences in the mechanical behavior of fissured rock. Consequently, these five parameters were fixed to investigate the influence of confining pressure and loading rate on the mechanical behavior of fissured rock. A fissured rock specimen with two pre-existing flaws was designed and produced according to the results of Yang et al. [73], a is 11 mm, α is 45°, l is 36 mm, and β is 16.9090° [32]. Under the condition that the structure of the pre-existing flaws is relatively symmetrical, the crack evolution and failure characteristics of the fissured rock under different confining pressures and loading rates can be understood. So, all the flaw parameters of n, a, α, l, and β in the considered geometry are given in detail in Fig. 3.

2.4. Experimental process

The indenters were used to fix the rock specimen on the MTS base, which was also beneficial to seal the specimen and the indenters using a plastic film to prevent the immersion of the hydraulic oil. Vaseline should be smeared evenly on both ends of the specimen to ensure fine coupling between the specimen and the indenters [74]. The uniaxial and triaxial compression experiments on rock specimens were carried out with the MTS815 system with a pre-stress of 0.5 kN [75]. The uniaxial compression on the specimen can be tested directly at a specified loading rate [76]. In triaxial compression,

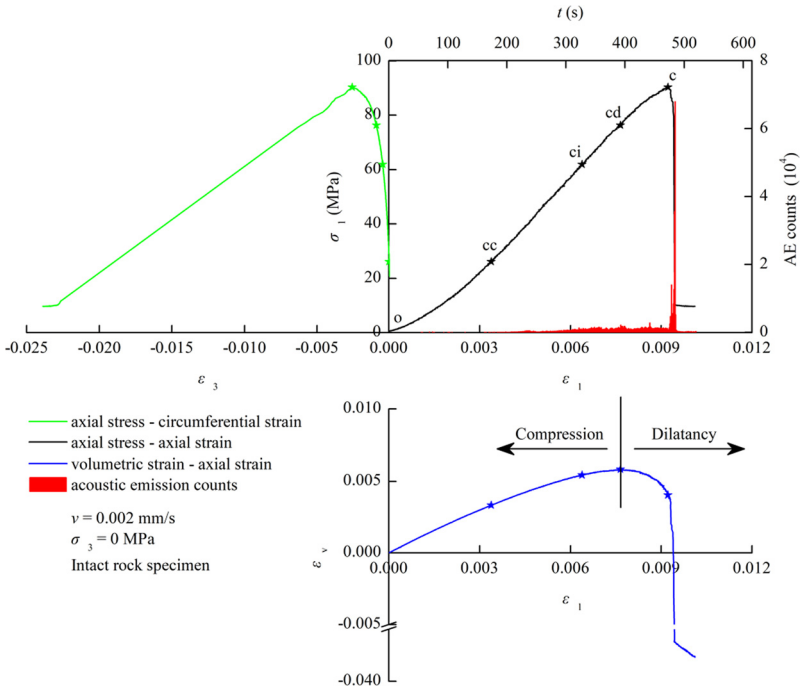

Fig. 4. Stress–strain curves of an intact rock specimen.

the confining pressure should keep a constant value before loading [69]. In this paper, the specified loading rates are 0.002, 0.02, and 0.2 mm/s, the confining pressures are 0, 1, 7, 13, and 19 MPa. The AE21C system should be worked while the compression starts.

3. Experimental results

In order to ensure the statistical validity of the test data, it is necessary to survey the homogeneity and dispersion among different rock specimens. Thus, a random group of specimens were selected to carry out the uniaxial compression test, including intact rock and fissured rock. For intact rock specimens, the uniaxial compressive strengths (UCSs) are 87.02, 91.00, 90.30, and 84.93 MPa, respectively, the average UCS is 88.31 MPa, and the coefficient of variation on UCS is 2.79%. For fissured rock specimens, the UCSs are 71.70, 76.07, and 73.56 MPa, respectively, the average UCS is 73.78 MPa, and the coefficient of variation on UCS is 2.43%. It presents small dispersion and fine homogeneity among those rock specimens, whether they are intact or fissured rocks.

Fig. 4 shows the stress–strain–AE curves of an intact rock specimen under uniaxial compression with a loading rate of 0.002 mm/s. The whole stress–strain behavior of the specimen can be divided into five stages with specific characteristics as follows.

(1) o-cc stage of pore compaction: the compactions of pores, microcracks, and weak planes in rock cause the production of few AE signals, and the axial stress–axial strain curve presents a concave shape in this stage. The circumferential strain is unvaried, the volumetric strain increases with compression.

(2) cc-ci stage of elastic deformation: all the axial strain, circumferential strain, and volumetric strain vary linearly in this stage. The mutual occlusion and friction of the weak planes in rock cause a gradual increase in AE activity.

(3) ci-cd stage of Initiation and stability propagation of crack: the ci point is usually the end point of the elastic deformation of the rock material, which can be obtained from the formula $E_s = E_{max} = \frac{\sigma_{ci}-\sigma_{cc}}{\varepsilon_{ci}-\varepsilon_{cc}}$. Moreover, Cai et al. [77] considered that the stress at the ci point can fracture the cohesive particles in the rock, so this point is also considered as the crack initiation threshold. The fracture and slippage of the deteriorative cohesive particles around the tips of those defects promote the propagation of cracks, which cause fluctuations in the AE signals and non-linear variation in the stress–strain curve.

(4) cd-c stage of damage and unstable propagation of cracks: the propagation of cracks intensifies with deformation, which greatly deteriorates the rock structure and results in a sharp increase in the AE signals. The circumferential strain increases rapidly. The criterion $\varepsilon_1 \geq |\varepsilon_2 + \varepsilon_2|$ always holds before the dilatancy onset of cd; however, it transforms into $\varepsilon_1 < |\varepsilon_2 + \varepsilon_2|$ after this point. Therefore, the volumetric strain starts to decrease, and the deformation is transformed from compression to dilatancy. This turning point is the dilatancy onset, and it is usually considered that irreversible damage occurs in the rock, which results in its rapid dilatancy and deformation.

(5) Failure stage: The cracks continuously propagate to form the macroscopic fracture planes, which results in an explosive increase in AE signals; obvious strain softening characteristics are observed.

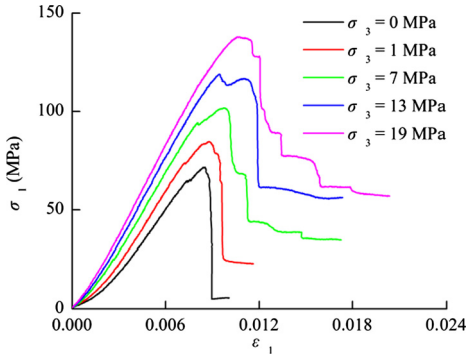

Fig. 5. Axial stress–axial strain curve of fissured rock specimens with different values of the confining pressure under a loading rate of 0.002 mm/s.

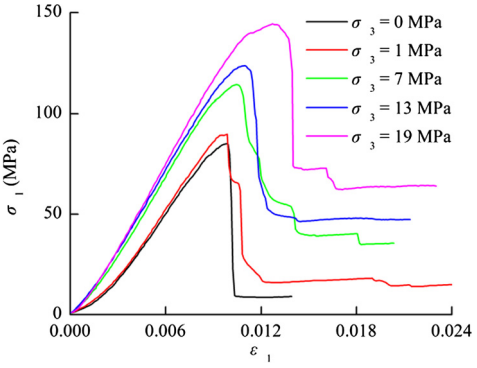

Fig. 6. Axial stress–axial strain curve of fissured rock specimens with different values of the confining pressure under a loading rate of 0.02 mm/s.

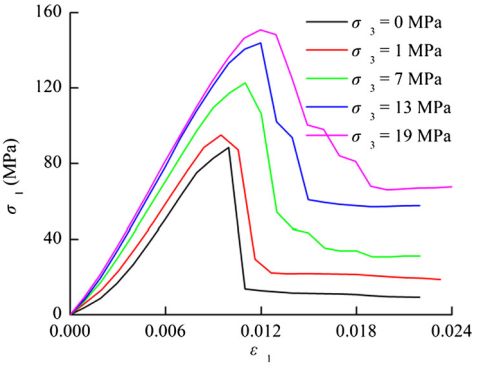

Fig. 7. Axial stress–axial strain curve of fissured rock specimens with different values of the confining pressure under a loading rate of 0.2 mm/s.

3.1. Stress–strain behaviors

Figs. 5, 6, and 7 show the axial stress–axial strain curves of a fissured rock specimen under different confining pressures and three kinds of loading rates. It is easy to see that all rock specimens are subjected to the above five stages during loading. The peak strength, the peak strain, and the elastic modulus are positively related to the confining pressure. In addition, under the lower loading rates of 0.002 and 0.02 mm/s, the fissured rock specimens present a significant phenomenon, which shows that the axial stress usually drops abruptly after the dilatancy onset. It is caused by crack propagation around the tips of the pre-existing flaws. Under high confining pressure, the fissured rock specimens present an obvious yield platform. Axial strain continues to increase under constant axial stress. Then the specimens gradually yield to failure around the inner tips of pre-existing flaws. However, under higher loading rates, such as 0.2 mm/s, similar phenomena are not evidenced.

3.2. AE characteristics

Figs. 8, 9, and 10 show the AE distributions of fissured rock specimens under different confining pressures and three kinds of loading rates. It is not difficult to see that the effect of the confining pressure on the AE activity in a fissured rock

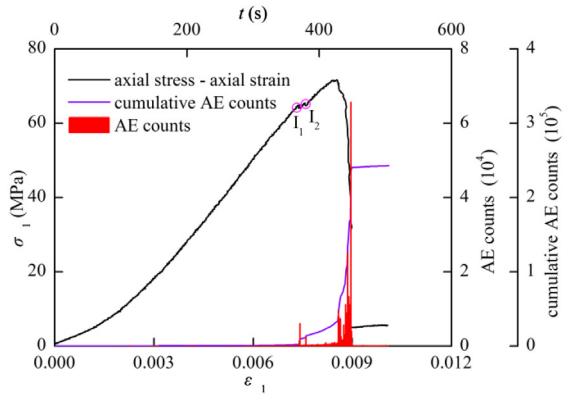

(a) σ_3 = 0 MPa

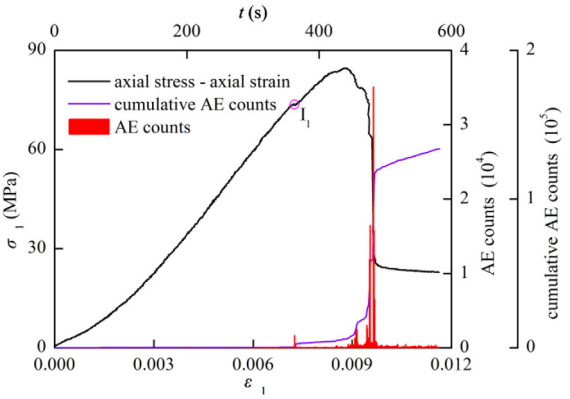

(b) σ_3 = 1 MPa

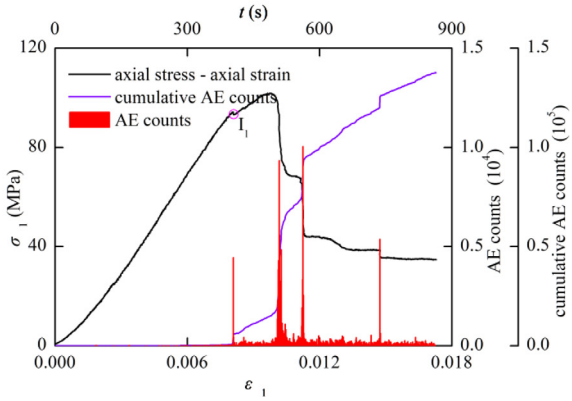

(c) σ_3 = 7 MPa

Fig. 8. AE distribution of fissured rock specimens with different values of the confining pressure under a loading rate of 0.002 mm/s.

specimen is mainly manifested after the dilatancy onset. Compared with the rock specimen under uniaxial compression, the existence of confining pressure causes that the rock specimen can still be loaded by fissure friction, even if the cohesive particles are fractured, which results in the full development of cracks after the dilatancy onset. So, the high AE signals in fissured rock after the dilatancy onset under high confining pressure can be explained. From Figs. 8d, 8e, 9d and 9e, the AE signals in rock specimens under confining pressures of 13 and 19 MPa after the dilatancy onset are obviously more active than those of other rock specimens. It should be noted that the varying degrees of stress drop are exhibited in the fissured rock specimens after the dilatancy onset under low loading rates. In this process, the AE signals increase sharply while the stress drops instantaneously; this indicates a large propagation or coalescence of cracks engendered in the rock. This point with stress drop is defined as I_i in the figures: the first point is I_1, and the second one is I_2. After the dilatancy onset, the yield platform is even emerged in the fissured rock specimen under high confining pressure, as shown in Figs. 8d and 8e. At this moment, the AE signals are extremely active, which indicates that crack evolution and propagation is extremely

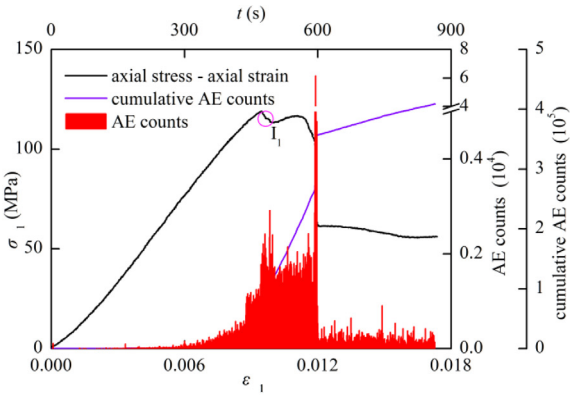

(d) σ_3 = 13 MPa

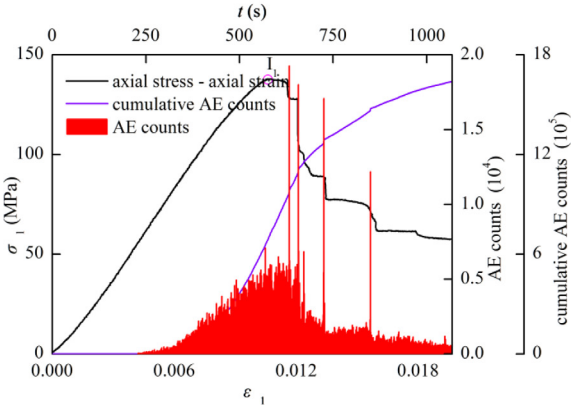

(e) σ_3 = 19 MPa

Fig. 8. (*continued*)

frequent. But the macroscopic failure will not occur in the specimen, which can still be loaded by friction among the fissures and the grains. In this process, more frictions and slippages among grains cause further propagation and even coalescence of cracks in the rock. With the increase of the loading rate, the I_i points are more difficult to characterize, but can still be identified by a sharp increase of AE signals, as shown in Fig. 9. Under a high loading rate of 0.2 mm/s, these specific phenomena, including stress drop and yield platform, do not occur. The AE signals are so little because of the too fast loading rate. However, the violent AE activities of the rock before the peak are mainly distributed in the cd-c stage, especially for the specimen under high confining pressure. Although the increase in confining pressure can strengthen the friction among grains to magnify the peak strength of geo-materials, the defects fully develop to cause potential hazards in deep rock engineering.

3.3. Strength characteristics

The Mohr–Coulomb strength criterion is usually applied to describe the strength characteristics of rock materials in rock engineering [78–82].

$$\sigma_{1c} = M + N\sigma_3 \tag{1}$$

$$M = 2c\frac{\cos\varphi}{1-\sin\varphi} \tag{2}$$

$$N = \frac{1+\sin\varphi}{1-\sin\varphi} \tag{3}$$

where M and N are the strength parameters of Mohr–Coulomb's strength criterion, c is the cohesive force, and φ is the internal friction angle.

The cohesive force of the rock material usually decreases with the yield of that material, which causes the fracture of cohesive particles. But it can still be loaded under the effect of fissure friction, the maximum friction force can exceed its cohesive force, and the friction force is correlated with the relative slippage of fissure friction (internal friction property) and

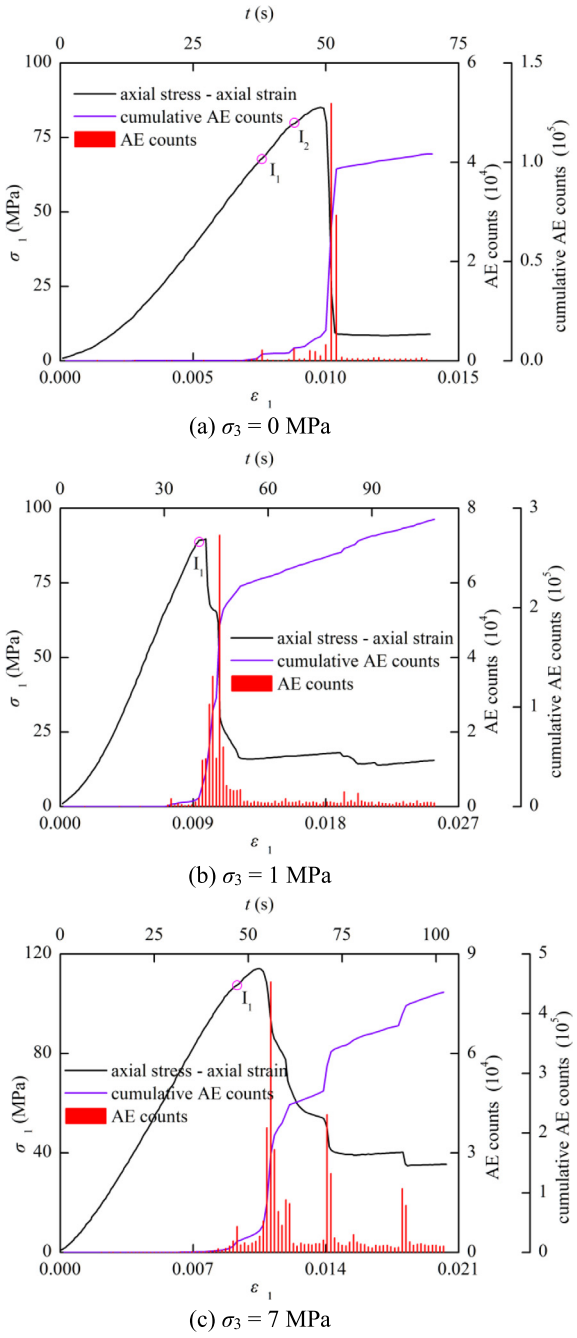

Fig. 9. AE distribution of fissured rock specimens with different values of the confining pressure under a loading rate of 0.02 mm/s.

external load [83]. Obviously, there is an upper limit of the friction force associated with the external load [84]. Under a high confining pressure, the shear force exceeds the cohesive force among the grains, causing the cohesive particles to fracture, and then the rock materials can still load through fissure friction. The increase of deformation can only yield more materials, but will not cause macroscopic slippage increasing the friction force. Consequently, there is an upper limit in the maximum shear stress (i.e. the principal stress difference) of rock materials. According to this, we construct the exponential strength criterion, which can preferably characterize the relation between the strength parameters and the confining pressures, and it also has clear physical meaning and mechanical concept [85]:

$$\sigma_{1c} - \sigma_3 = F - f_1 e^{-f_2 \sigma_3} \tag{4}$$

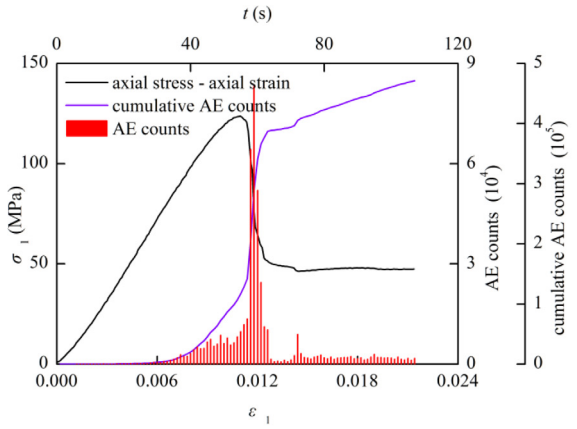

(d) $\sigma_3 = 13$ MPa

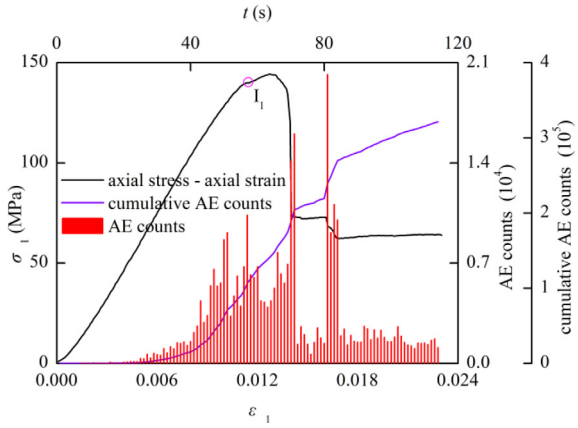

(e) $\sigma_3 = 19$ MPa

Fig. 9. (*continued*)

where F, f_1, and f_2 are the strength parameters of the exponential strength criterion, F is the maximum principal stress difference.

Therefore, the linear and exponential functions can be used to describe the relationships between the strength parameters of the rock material at the specific points of dilatancy onset and peak point and the confining pressures:

$$\sigma_s = M + N\sigma_3 \tag{5}$$

$$\sigma_s - \sigma_3 = F - f_1 e^{-f_2\sigma_3} \tag{6}$$

where σ_s is the strength parameter of the rock material at dilatancy onset or peak point; at dilatancy onset, $\sigma_s = \sigma_{1cd}$, at peak point, $\sigma_s = \sigma_{1c}$.

Fig. 11 shows the relations between the strength parameters (stress of dilatancy onset and peak strength) and the confining pressures under three kinds of loading rates, and the corresponding relationships are given in Table 4. Obviously, the strength parameters of fissured rock are positively related to the confining pressure. Table 5 presents the strength parameters of fissured rock under the two strength criteria of the Mohr–Coulomb strength criterion and the exponential strength criterion. It can be seen that the cohesive force c and the maximum principal stress difference F obtained from the peak points are all larger than those obtained from the dilatancy onsets. However, the internal friction angle φ obtained from the dilatancy onsets is larger than that obtained from the peak points. The cohesive force c and the maximum principal stress difference F of the fissured rock are positively correlated with the loading rate, but the internal friction angle φ is negatively correlated with the loading rate, whether at the peak points or the dilatancy onsets. Thus, the cohesion and internal friction properties of fissured rock are significantly related to the loading rate.

Under loading rates of 0.002 and 0.02 mm/s, the Mohr–Coulomb strength criterion and the exponential strength criterion can characterize the relations between the strength parameters and the confining pressures, but the correlation of the exponential strength criterion is higher than that of the Mohr–Coulomb strength criterion. Under a loading rate of 0.2 mm/s, the correlation between the exponential strength criterion and the strength parameters is significantly higher than that of Mohr–Coulomb's strength criterion. Moreover, when the confining pressure is 0 MPa, the formulas (5) and (6) have a clear

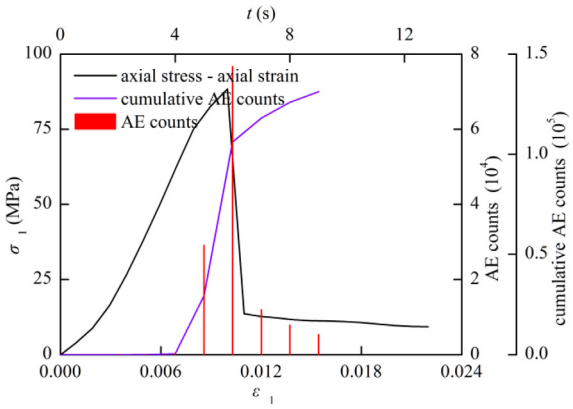

(a) $\sigma_3 = 0$ MPa

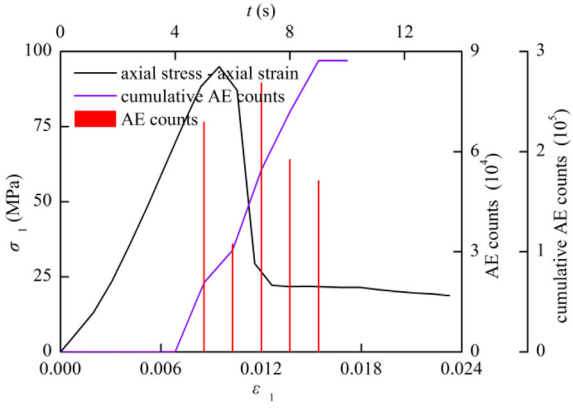

(b) $\sigma_3 = 1$ MPa

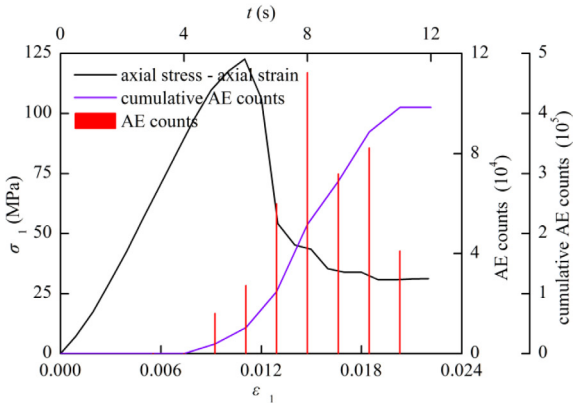

(c) $\sigma_3 = 7$ MPa

Fig. 10. AE distribution of fissured rock specimens with different values of the confining pressure under a loading rate of 0.2 mm/s.

physical meaning, which characterizes the strength at a specific point. Moreover, the strength parameters obtained from the exponential strength criterion are significantly closer to the experimental values than those got from the Mohr–Coulomb strength criterion, both at the peak points and the dilatancy onsets. In fact, the increase in the rate of maximum shear stress gradually decreases with increasing the confining pressure, and the relation between the maximum shear stress and the confining pressure is not linear, which can be characterized by a more suitable exponential function. Therefore, it is shown that the exponential strength criterion is more suitable for characterizing the strength parameters of fissured rock.

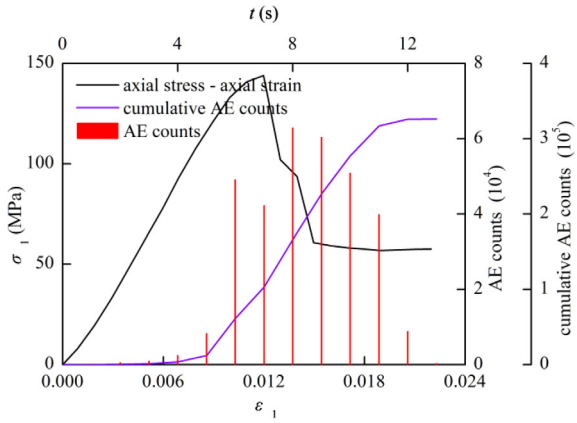

(d) σ_3 = 13 MPa

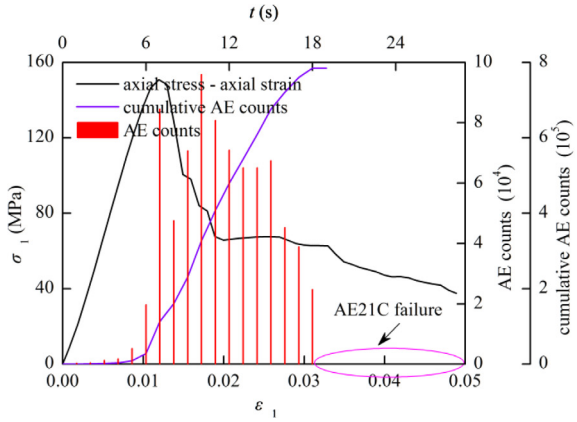

(e) σ_3=19 MPa

Fig. 10. (*continued*)

3.4. Failure characteristics

In order to distinguish the failure characteristics of fissured rock specimens under different confining pressures and loading rates, it is necessary first to discuss the failure characteristics of intact rock specimens under the same conditions. According to the results of Wong and Einstein [43], Huang et al. [86], Yang et al. [71,73], and Zhang and Wong [49], the type of the initiated crack can be easily judged. Therefore, Fig. 12 gives the failure characteristics of intact rock specimens. It is easy to see that the failure mode of an intact rock specimen under uniaxial compression with a loading rate of 0.002 mm/s shows a typical axial splitting. There is an obvious tensile coalescence with some small secondary tensile cracks in this specimen. Under a confining pressure of 1 MPa, due to the small confining pressure, the rock specimen still shows an obvious tensile failure mode, but some lateral tensile cracks have begun to initiate locally. Under confining pressures of 7 and 13 MPa, the rock specimens present an obvious tensile shear coalescence mode, and the tensile cracks occur near the main shear crack and the ends of the specimens. Under a confining pressure of 19 MPa, the lateral tensile cracks are initiated around the main tensile and main shear cracks of the rock specimen. It is not difficult to see that the crack coalescence mode of an intact rock specimen tends to be complicated with increasing the confining pressure: tensile coalescence gradually transforms into tensile shear coalescence. Under uniaxial compression, more secondary tensile cracks and lateral tensile cracks are generated with increasing the loading rate, and crack branching is even present in that specimen under a loading rate of 0.2 mm/s. Under a confining pressure of 19 MPa with loading rates of 0.02 and 0.2 mm/s, there is a significant main shear crack, parts with lateral tensile cracks, secondary tensile cracks, and secondary shear cracks. Thus, the effect of increasing the loading rate on the crack evolution of an intact rock specimen under uniaxial compression seems to be greater than that with triaxial compression.

Fig. 13 presents the failure characteristics of fissured rock specimens. It is easy to see that the failure mode of a fissured rock specimen shows tensile shear coalescence under uniaxial compression with a loading rate of 0.002 mm/s. The crack firstly initiates in the tensile stress concentration zone around the tips of the pre-existing flaws, then propagates and extends to the ends of the specimen along the axial loading direction. The specific phenomenon of stress drop occurs with a large propagation of crack, but the rock specimen does not fail instantaneously, that is at I_1 point. Then the main cracks, such as tensile cracks and shear cracks, gradually evolve to connect with the cracks initiated from the tips of the pre-existing flaws.

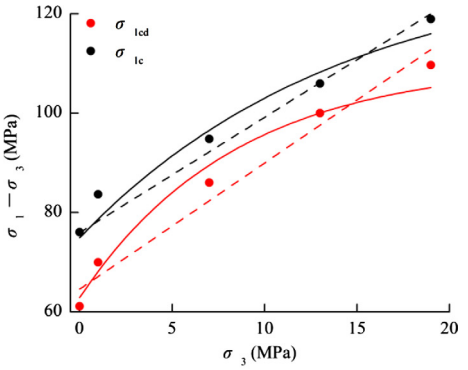

(a) loading rate of 0.002 mm/s

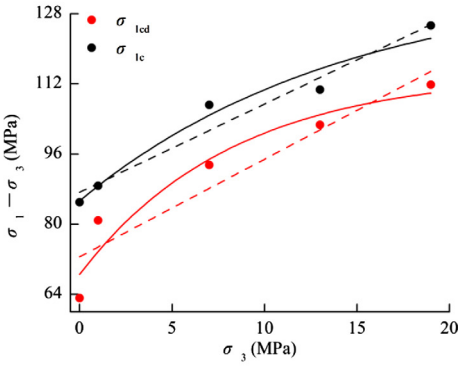

(b) loading rate of 0.02 mm/s

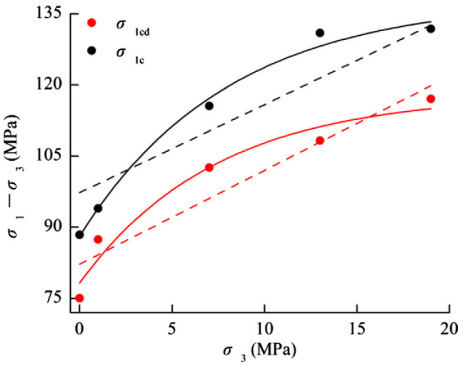

(c) loading rate of 0.2 mm/s

Fig. 11. Relations between strength parameters and confining pressures under different loading rates.

Table 4
Relationships between strength parameters and confining pressures under different loading rates.

Loading rate (mm/s)	Specific point	Type	Relationship	Correlation coefficient
0.002	Dilatancy onset	Linearity	$\sigma_{1cd} = 3.5371\sigma_3 + 64.6040$	0.9719
		Exponential	$\sigma_{1cd} - \sigma_3 = 110.1139 - 47.2380e^{-0.1185\sigma_3}$	0.9782
	Peak point	Linearity	$\sigma_{1c} = 3.3193\sigma_3 + 75.9813$	0.9628
		Exponential	$\sigma_{1c} - \sigma_3 = 130.7968 - 55.8854e^{-0.0699\sigma_3}$	0.9660
0.02	Dilatancy onset	Linearity	$\sigma_{1cd} = 3.2256\sigma_3 + 72.5913$	0.8477
		Exponential	$\sigma_{1cd} - \sigma_3 = 114.5488 - 45.9811e^{-0.1206\sigma_3}$	0.8758
	Peak point	Linearity	$\sigma_{1c} = 3.0131\sigma_3 + 87.2919$	0.9428
		Exponential	$\sigma_{1c} - \sigma_3 = 135.8366 - 50.4909e^{-0.0697\sigma_3}$	0.9549
0.2	Dilatancy onset	Linearity	$\sigma_{1cd} = 2.9808\sigma_3 + 82.2435$	0.8675
		Exponential	$\sigma_{1cd} - \sigma_3 = 118.0820 - 39.8216e^{-0.1353\sigma_3}$	0.9286
	Peak point	Linearity	$\sigma_{1c} = 2.8576\sigma_3 + 97.3272$	0.8634
		Exponential	$\sigma_{1c} - \sigma_3 = 138.0103 - 49.8295e^{-0.1248\sigma_3}$	0.9846

Table 5
Strength parameters of the fissured rock specimens.

v (mm/s)	Dilatancy onset						Peak point					
	Mohr–Coulomb strength criterion			Exponential strength criterion		Experimental result	Mohr–Coulomb strength criterion			Exponential strength criterion		Experimental result
	σ_{1cd} when $\sigma_3 =$ 0 MPa (MPa)	c (MPa)	φ (°)	σ_{1cd} when $\sigma_3 =$ 0 MPa (MPa)	F (MPa)	σ_{1cd} when $\sigma_3 =$ 0 MPa (MPa)	σ_{1c} when $\sigma_3 =$ 0 MPa (MPa)	c (MPa)	φ (°)	σ_{1c} when $\sigma_3 =$ 0 MPa (MPa)	F (MPa)	σ_{1c} when $\sigma_3 =$ 0 MPa (MPa)
0.002	64.60	17.18	34.00	62.88	110.11	62.69	75.98	20.85	32.48	74.91	130.80	73.78
0.02	72.59	20.21	31.78	68.57	114.55	63.11	87.29	25.14	30.11	85.35	135.84	85.03
0.2	82.24	23.82	29.84	78.26	118.08	75.02	97.33	28.79	28.79	88.18	138.01	88.44

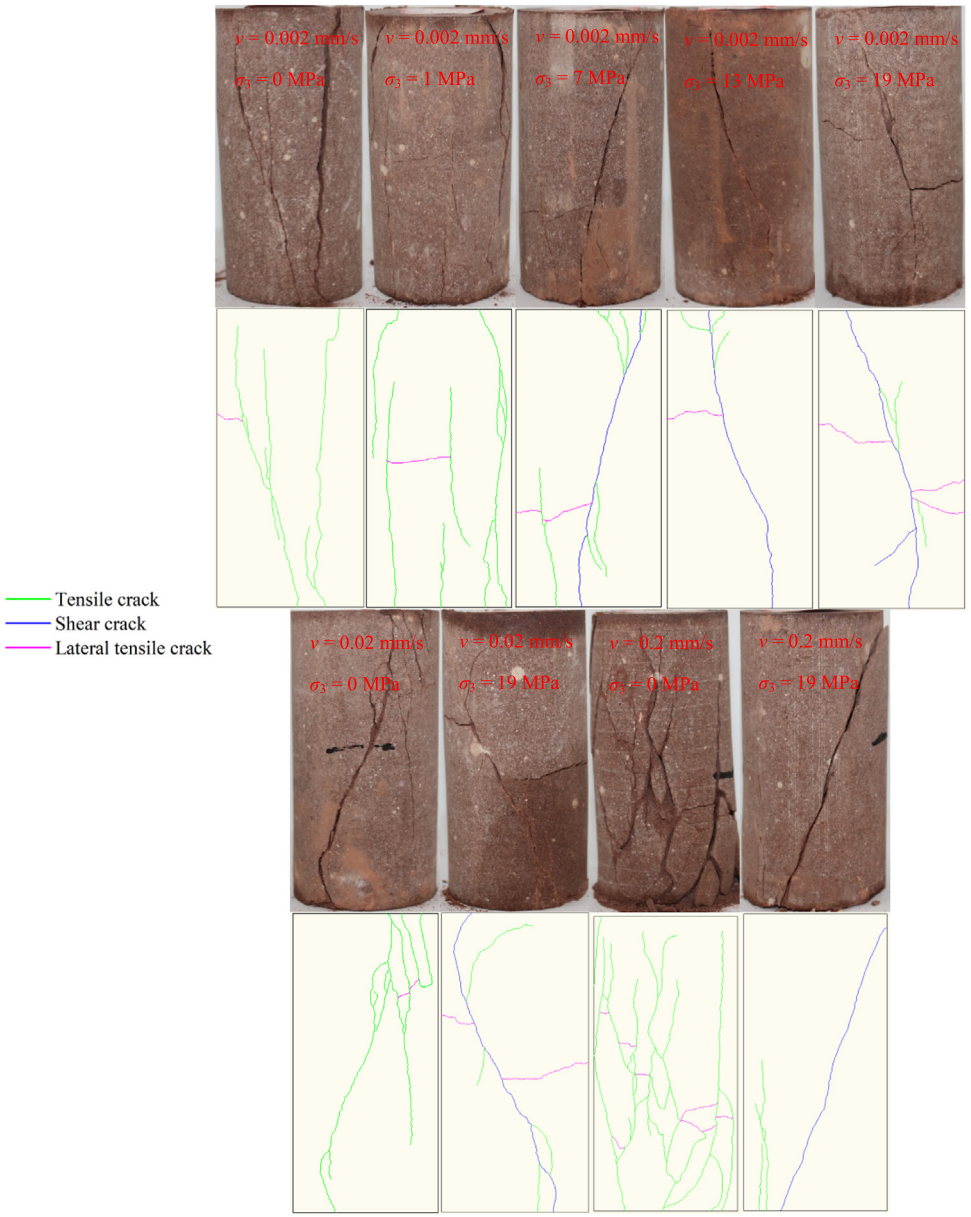

Fig. 12. Failure characteristics of intact rock specimens.

With increasing the loading rate, the number of cracks initiated near the tips of the pre-existing flaws not only increase, but also the obvious crack branching is observed. The lateral tensile cracks occur between the two pre-existing flaws, as shown in Fig. 13I-I, Fig. 13II-I, and Fig. 13III-I. Surface spalling caused by the interlaced connections of the multiform cracks is worse with increasing the loading rate. Thus, it is easy to see that the crack evolution and failure mode of fissured rock under uniaxial compression are more complicated than those of an intact rock. With increasing the confining pressure, the fissured rock presents characteristics of multi-section failure, the tensile cracks are also initiated from the tips of pre-existing flaws, and the crack branching is accompanied by the higher loading rate. The primary fissures and the new cracks are compacted and closed, and then the rock material can be loaded by friction among the grains in the rock, where the friction force is greater than the cohesive force among the cohesive particles of rock. At this point, the original damages to cohesive particles in rock are prone to provoke shear fracture, which causes the formation of shear cracks between two or among more tensile cracks. Lateral tensile cracks are also accompanied by coalescence connections of main shear cracks and main tensile cracks. The multiple main shear cracks connect with the tensile cracks initiated from the tips of the pre-existing flaws to make the rock fail, as in Fig. 13II-V. Consequently, the failure mode of fissured rock is characterized by multi-section coalescence, as shown in Fig. 14. The interlaced connections of the multiform cracks cause surface spalling (Fig. 13). The obvious traces left

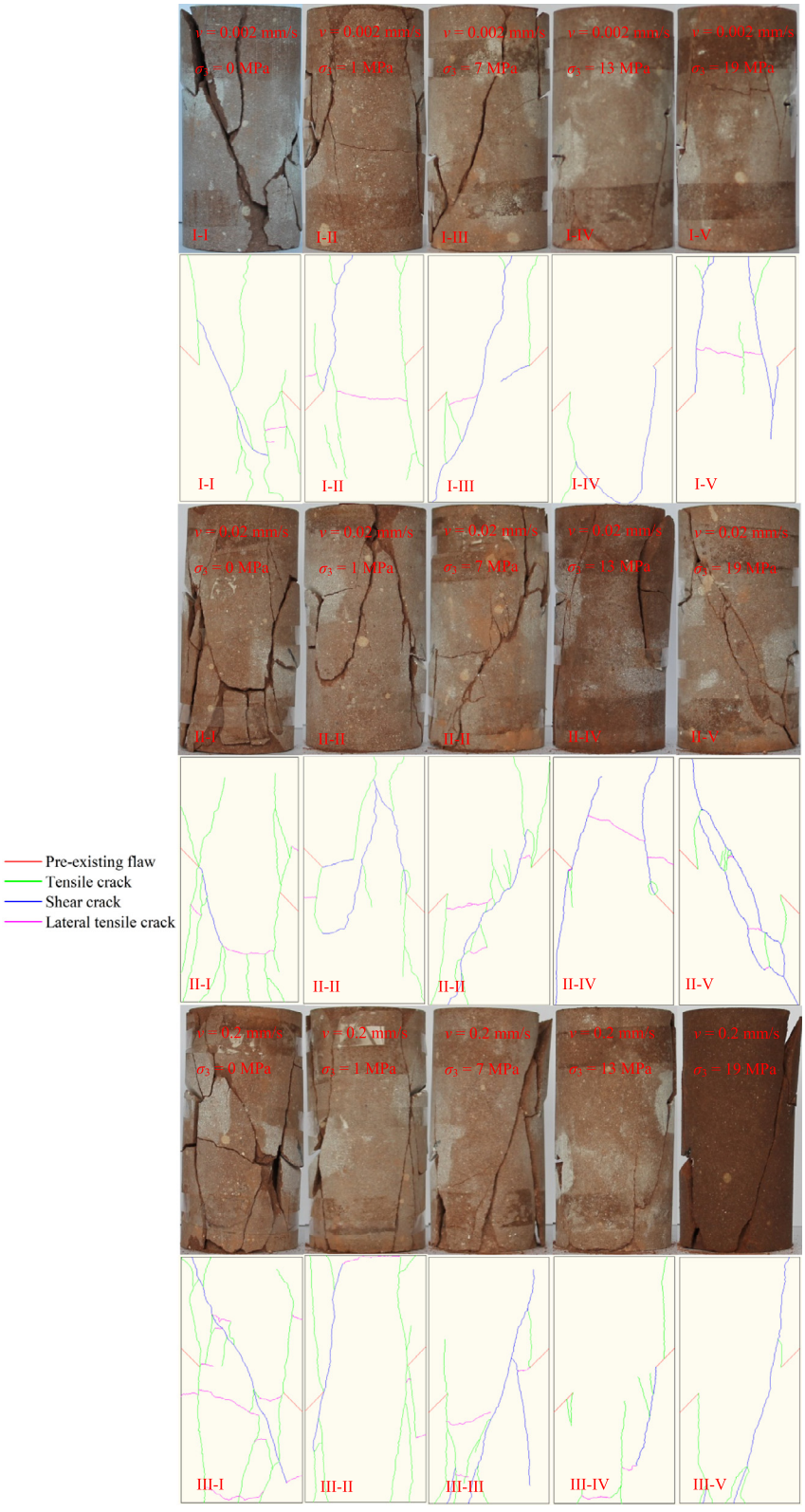

Fig. 13. Failure characteristics of fissured rock specimens.

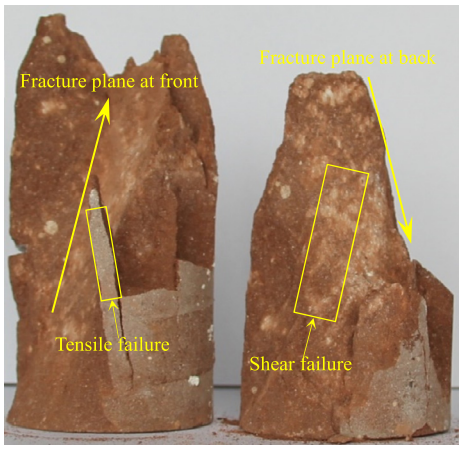

Fig. 14. Fracture plane of fissured rock specimens.

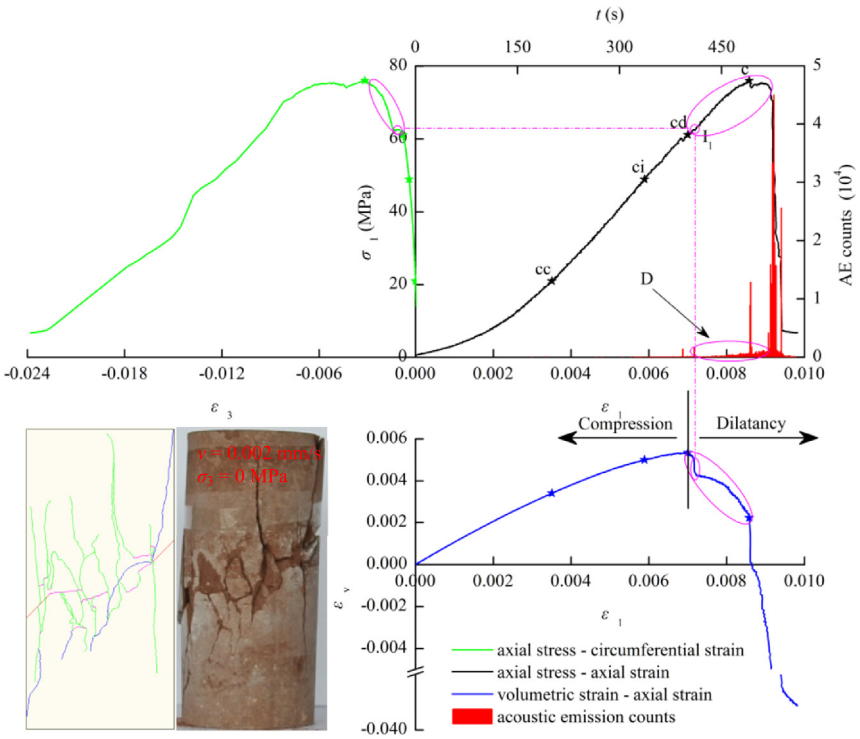

Fig. 15. Special failure characteristics of a fissured rock specimen.

by the friction slippage of grains on the shear fracture plane can be easily seen in Fig. 14. So, the load capacity of a fissured rock specimen depends on the crack evolution around the tips of the pre-existing flaws and the friction among the grains of the rock materials.

It is worth noting that Fig. 15 shows different failure characteristics under the same conditions than Fig. 13I-I. A large amount of tensile, lateral tensile and shear cracks are fully developed between the two pre-existing flaws, and multiple surface spallings are formed by these cracks. This also supports the above view. These cracks are mostly initiated after the dilatancy onset, the I_1 point appearing in the figure corresponds to larger crack initiation, meanwhile the AE signals, circumferential strain, and volumetric strain increase sharply.

4. Discussion

The evolution, propagation and even coalescence of cracks in fissured rock cause the deterioration of its strength and deformation, which seriously affects its engineering behavior. However, the multiple factors that can affect the mechanical

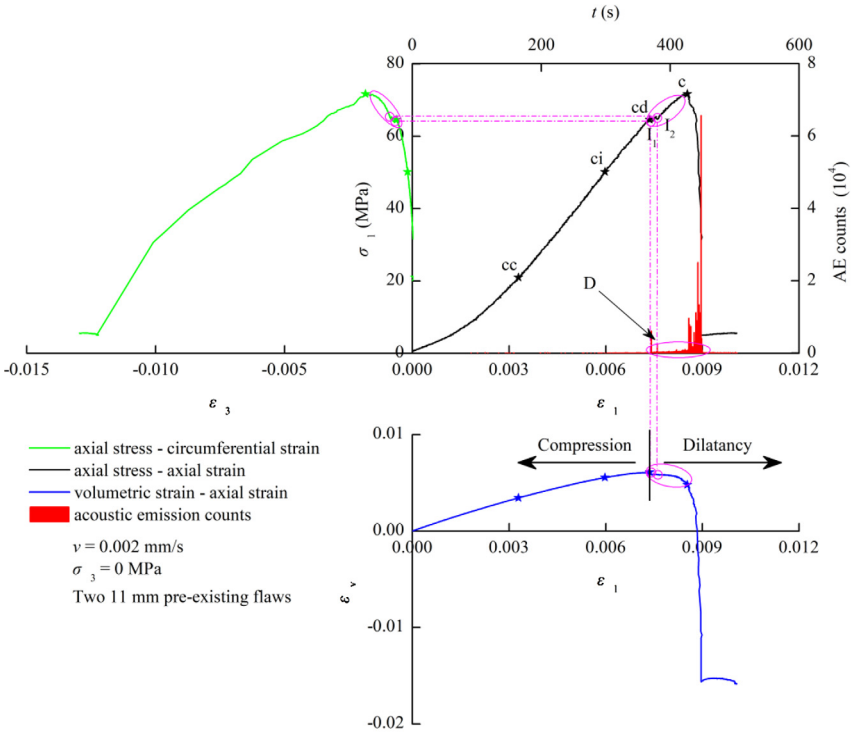

(a) $\sigma_3 = 0$ MPa

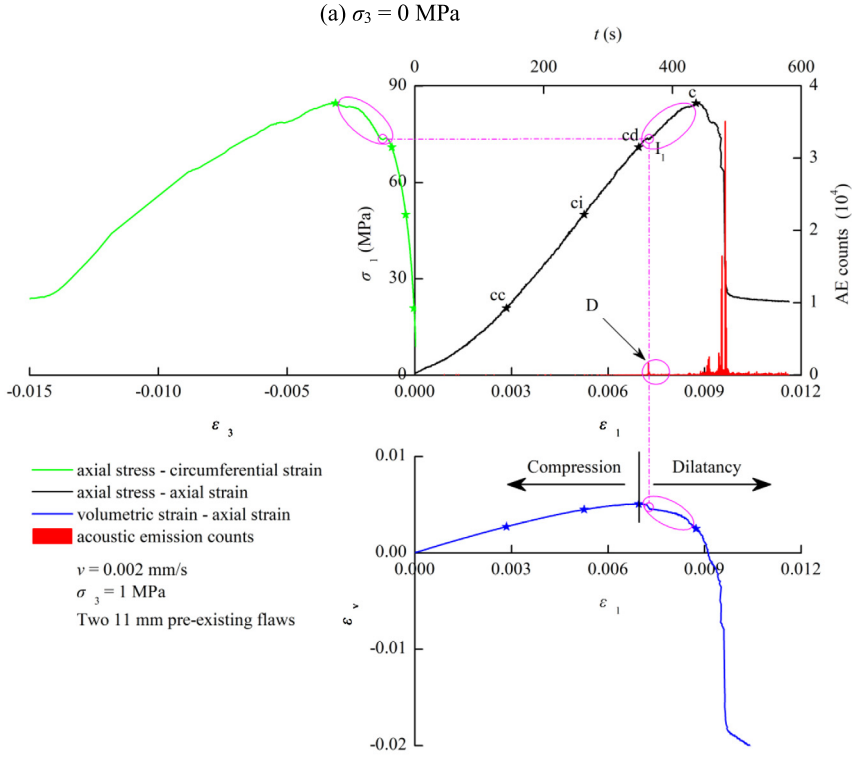

(b) $\sigma_3 = 1$ MPa

Fig. 16. Stress–strain–AE curves of fissured rock specimens with different confining pressures under a loading rate of 0.002 mm/s.

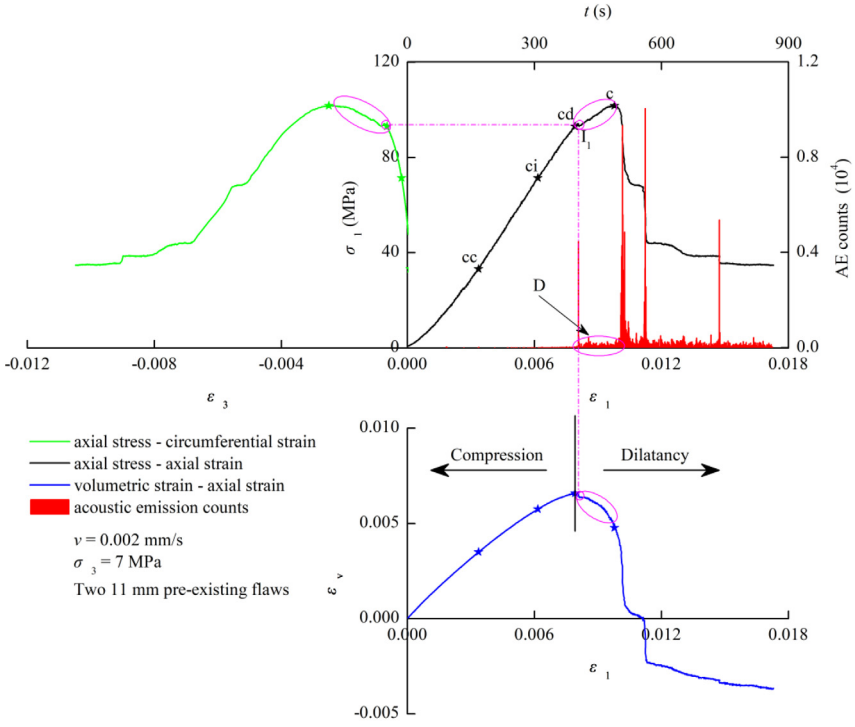

(c) σ_3 = 7 MPa

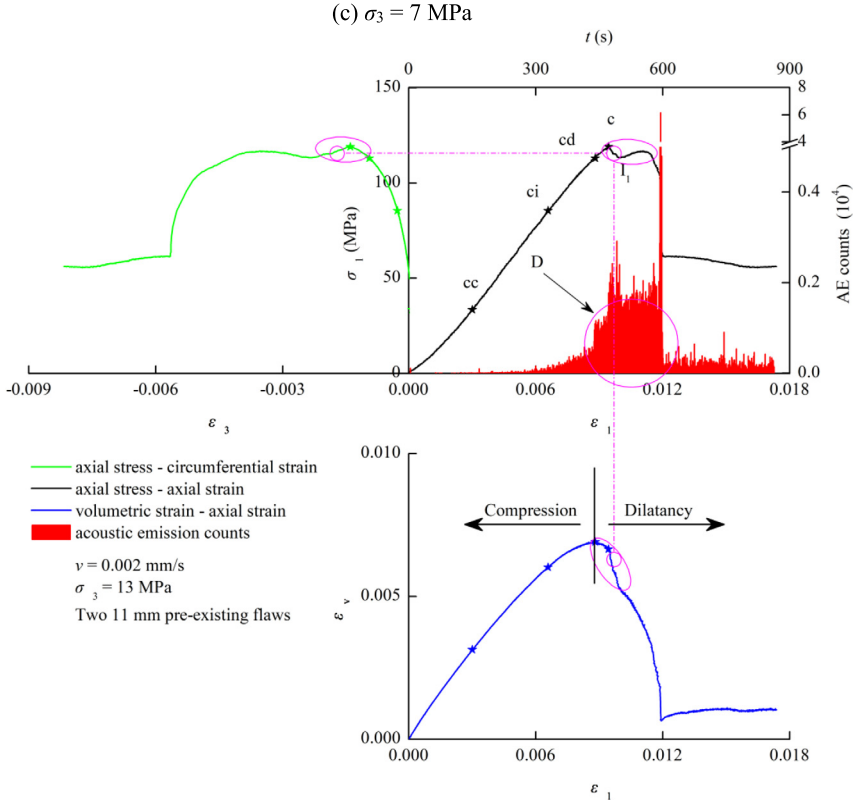

(d) σ_3 = 13 MPa

Fig. 16. (*continued*)

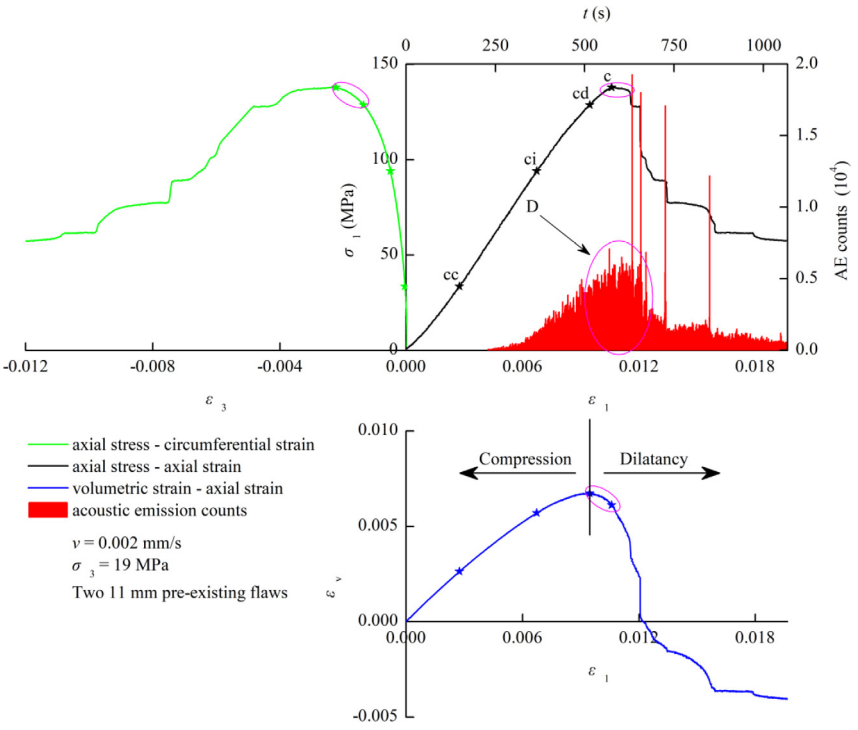

(e) σ_3 = 19 MPa

Fig. 16. (*continued*)

behavior of fissured rock cause a failure in the engineering parameter. Hence, Martin and Chandler [87] used 50% of unconfined compressive strength as the strength parameter of rock mass in engineering to improve its stability. However, it is just an empirical criterion, which has no clear physical meaning. Consequently, Figs. 16, 17, and 18 plot the stress–strain–AE curves of fissured rock specimens with different confining pressures under three kinds of loading rates to characterize their dilatancy behavior, in order to attempt to obtain reasonable strength parameters in engineering from the investigation of the dilatancy behavior of fissured rock. Compared with the intact rock specimen of Fig. 4, in addition to the deterioration of the mechanical parameters of fissured rock, the phenomenon of sharp increase in deformation after the dilatancy onset should be paid attention to by geotechnical scientists. Under the low loading rates of 0.002 and 0.02 mm/s, the obvious stress drop points I_i occurred, but the specimen did not fail instantaneously, and the AE signals, circumferential strain, and volumetric strain increased abruptly. The D regions in Figs. 16, 17, and 18 indicate that large crack propagation and coalescence occurred. Especially for the fissured rock specimens under the high confining pressure, the variation rates of circumferential strain and volumetric strain increase rapidly after the dilatancy onset, as shown in Fig. 16d and Fig. 17e, and yield platforms are even observed in Figs. 16d and 16e. Meanwhile, axial stress can keep an almost constant value with deformation, circumferential strain and volumetric strain increase with a high variation rate, and the volume of specimen dilates significantly. Under high loading rates, such as 0.2 mm/s, there is no stress drop or yield platform, but the deformation of fissured rock after the dilatancy onset is more pronounced than that under a low loading rate. The dilatancy behavior characterized by volumetric strain variation is positive with respect to the loading rate. In the case of fissured rock specimens under uniaxial compression with 0.002 mm/s, the volumetric strain, i.e. $\varepsilon_{vcd} = 6.09 \times 10^{-3}$ at dilatancy onset, varies to $\varepsilon_{vc} = 4.81 \times 10^{-3}$ at the peak point; the relative variation is $\Delta\varepsilon = 1.28 \times 10^{-3}$, as shown in Fig. 16a. At a loading rate of 0.02 mm/s, the volumetric strain $\varepsilon_{vcd} = 5.30 \times 10^{-3}$ at dilatancy onset varies to $\varepsilon_{vc} = 0.47 \times 10^{-3}$ at the peak point; the relative variation is $\Delta\varepsilon = 4.83 \times 10^{-3}$, as shown in Fig. 17a. At a loading rate of 0.2 mm/s, the volumetric strain $\varepsilon_{vcd} = 5.88 \times 10^{-3}$ at dilatancy onset varies to $\varepsilon_{vc} = -0.65 \times 10^{-3}$ at the peak point, the relative variation being $\Delta\varepsilon = 6.53 \times 10^{-3}$, as shown in Fig. 18a. In fact, it is easy to see that the main crack has begun to initiate and propagate after the dilatancy onset by the failure mode of fissured rock specimens. Especially, at high confining pressure and high loading rate, the more serious crack branching and mixed failure mode with multi-section formed by interlaced coalescence of multi-crack are more obvious. It is shown that the evolution of defects in rock after the dilatancy onset greatly dilates the volume of rock, which easily fractures the rock structure, resulting in engineering disasters. Especially rock engineering under high confining pressure and high loading rate is more prone to incur potential hazards.

It is worth noting that those large deformation phenomena in rock always occurred after the dilatancy onset, whether under high confining pressure or high loading rate, which indicates that the stress of dilatancy onset can be seen as the engineering parameter to consider in order to avoid large deformation and failure of rock mass.

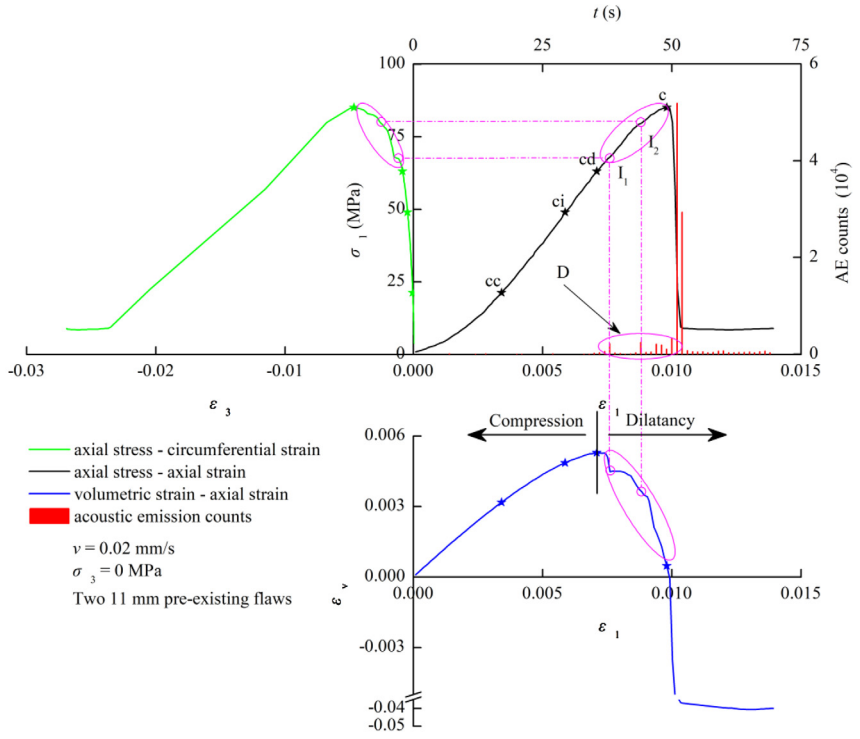

(a) $\sigma_3 = 0$ MPa

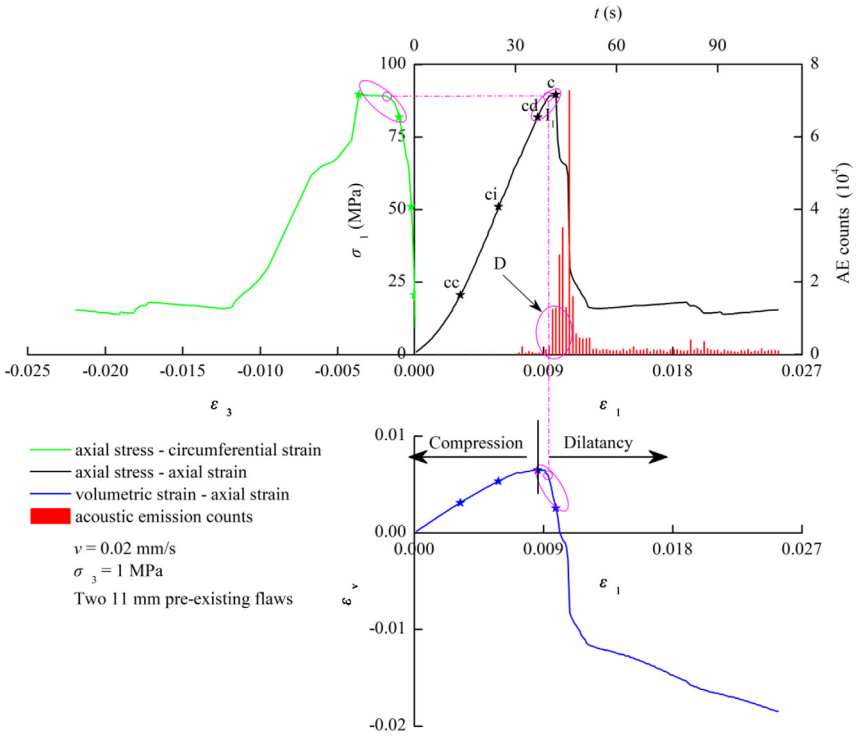

(b) $\sigma_3 = 1$ MPa

Fig. 17. Stress–strain–AE curves of fissured rock specimens with different confining pressures under a loading rate of 0.02 mm/s.

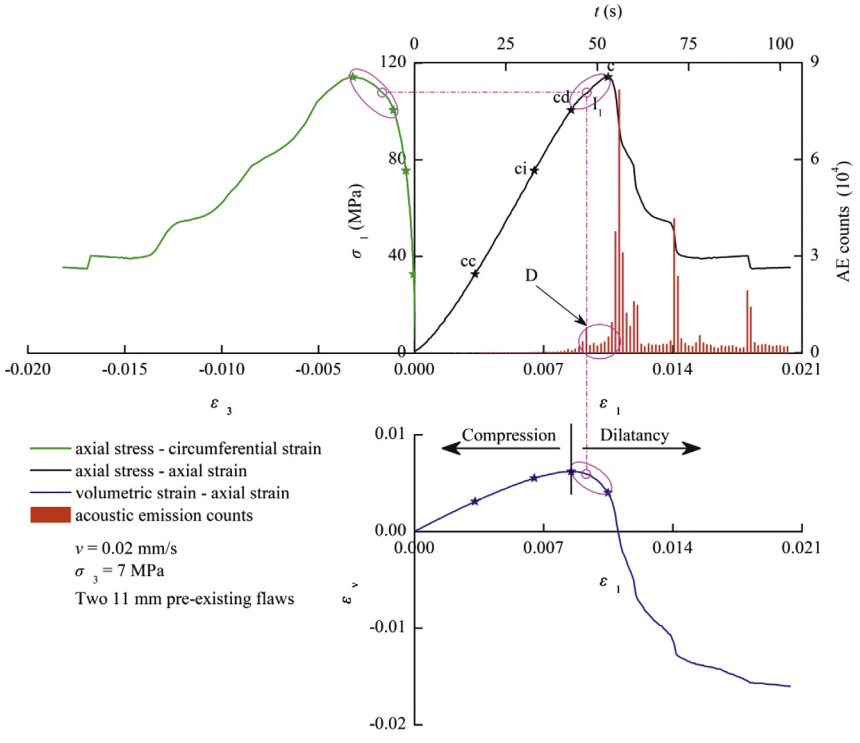

(c) σ_3 = 7 MPa

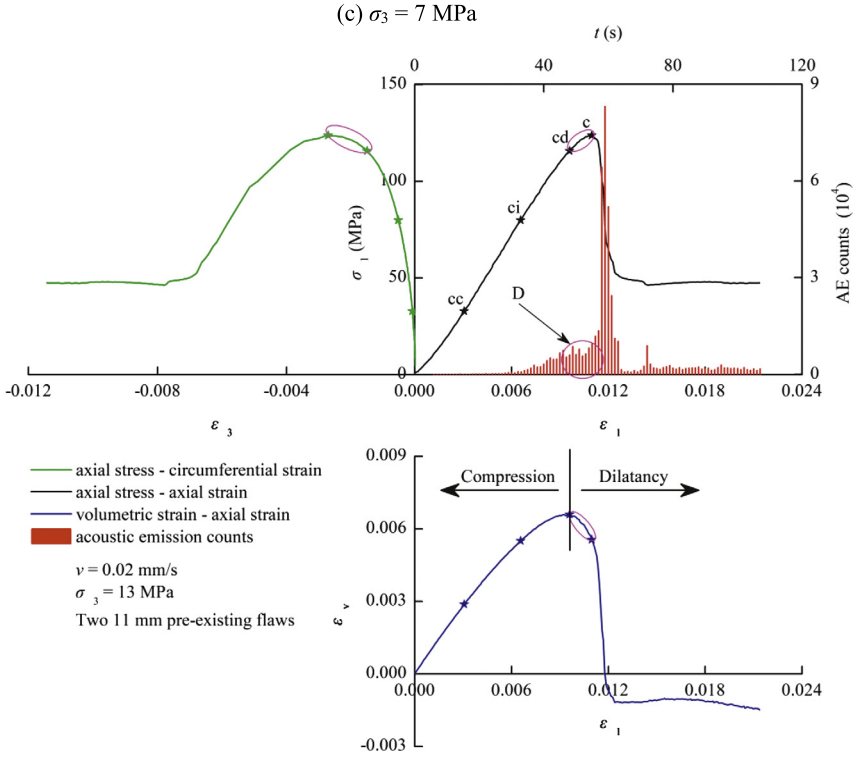

(d) σ_3 = 13 MPa

Fig. 17. (*continued*)

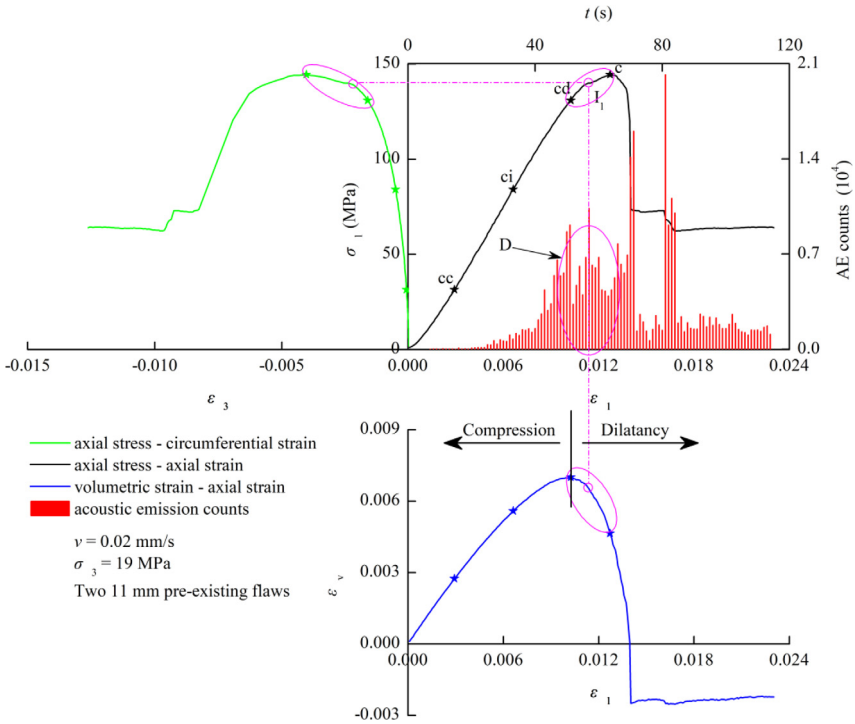

(e) σ_3 = 19 MPa

Fig. 17. (*continued*)

5. Conclusions

In this paper, the uniaxial and triaxial compression experiments with AE monitoring under different loading rates were carried out on the fissured rock specimens with the same geometrical distribution of two pre-existing flaws. The dilatancy and AE activity of those specimens were discussed, and the effects of the confining pressure and loading rate on the mechanical parameters and failure characteristics were analyzed.

(1) The strength parameters and the deformation parameters of fissured rock specimens increase with the confining pressure. The exponential strength criterion is more suitable than the Mohr–Coulomb strength criterion to characterize the strength characteristics of fissured rock.

(2) The crack evolution and failure characteristics of fissured rock specimens are more complicated than those of intact rock specimens. The failure characteristics of fissured rock follow the tensile shear coalescence model; the cracking occurs with increasing the loading rate, and the multi-section coalescence model is evidenced with increasing the confining pressure.

(3) The phenomena of stress drop and yield platform usually occurred after the dilatancy onset; the specimen does not fail instantaneously, and the propagation and coalescence of cracks cause a sharp increase in the AE signals, circumferential strain, and volumetric strain. This indicates that the stress of dilatancy onset can be seen as the engineering parameter to consider in order avoid large deformation and failure of rock mass.

6. Author contributions

Wu Jiangyu and Feng Meimei conceived and designed the experiments; Wu Jiangyu, Han Guansheng, and Yao Benyu performed the experiments; Wu Jiangyu, Feng Meimei, Han Guansheng and Ni Xiaoyan analyzed the data; Wu Jiangyu and Feng Meimei wrote the paper.

Acknowledgements

This work was supported by the Fundamental Research Funds for the Central Universities (2018BSCXB22) and the Postgraduate Research & Practice Innovation Program of Jiangsu Province (KYCX18_1970).

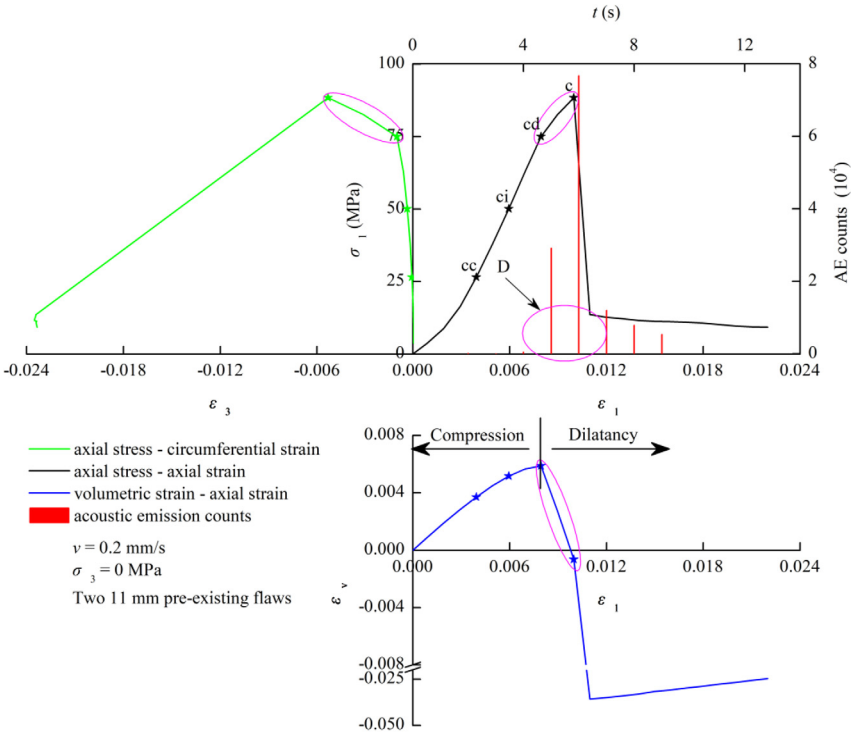

(a) σ_3 = 0 MPa

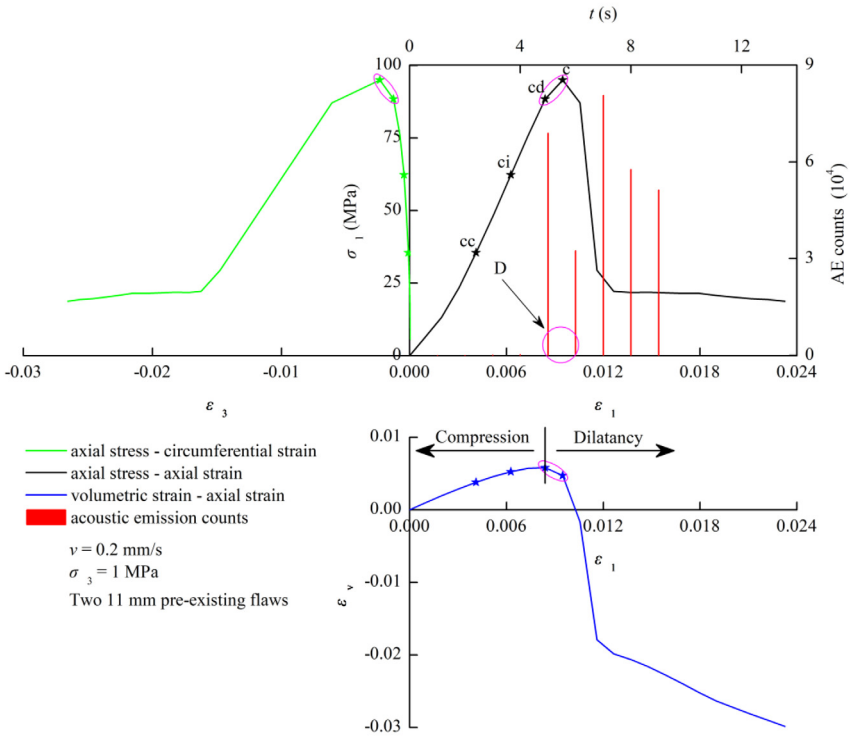

(b) σ_3 = 1 MPa

Fig. 18. Stress–strain–AE curves of fissured rock specimens with different values of the confining pressure under a loading rate of 0.2 mm/s.

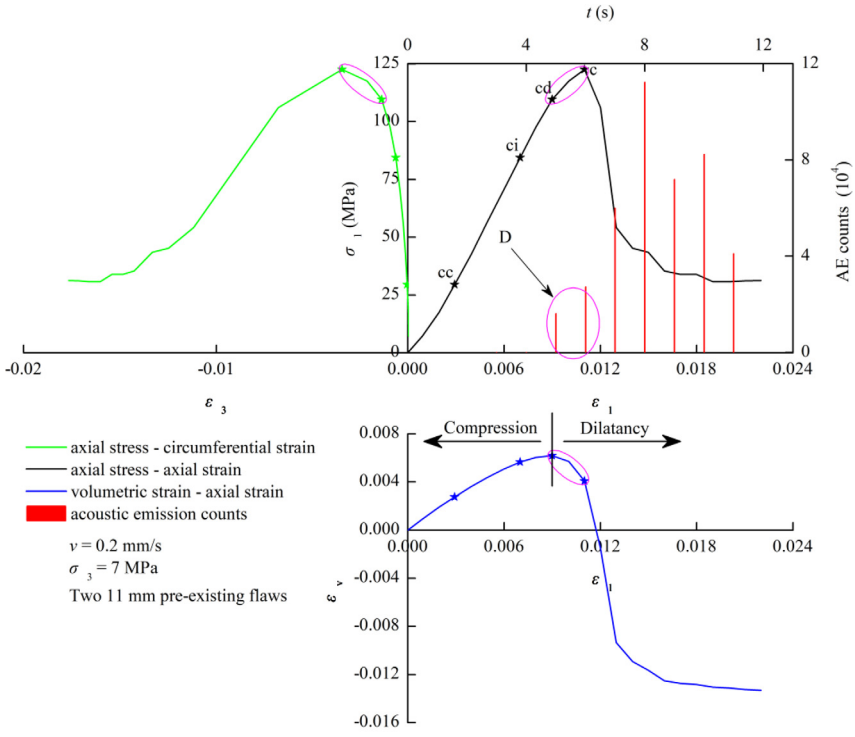

(c) $\sigma_3 = 7$ MPa

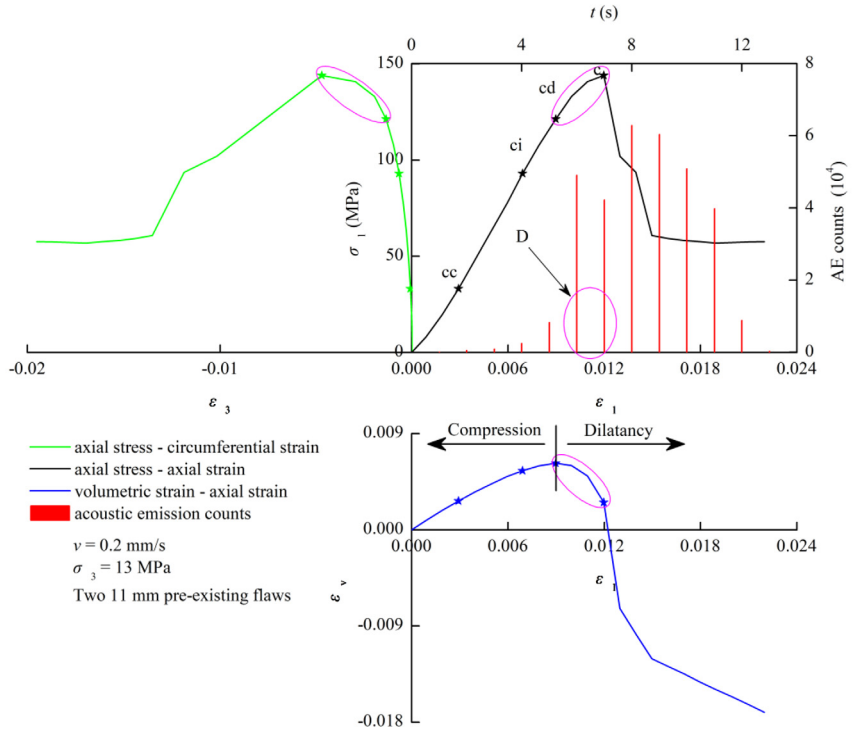

(d) $\sigma_3 = 13$ MPa

Fig. 18. (*continued*)

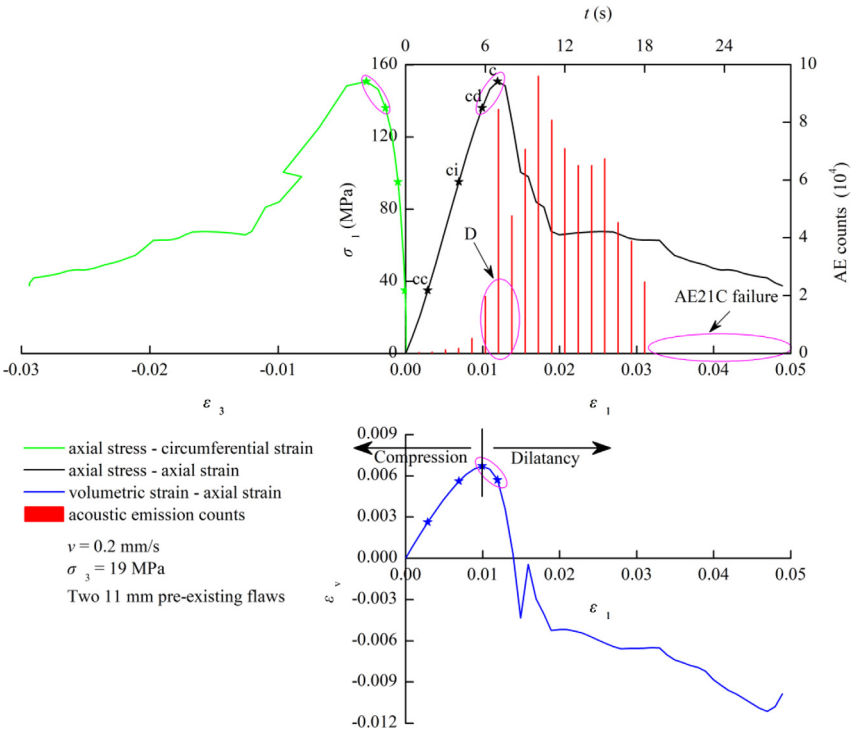

(e) σ_3 = 19 MPa

Fig. 18. (*continued*)

References

[1] M. Brideau, M. Yan, D. Stead, The role of tectonic damage and brittle rock fracture in the development of large rock slope failures, Geomorphology 103 (1) (2009) 30–49.

[2] P. Cao, T. Liu, C. Pu, H. Lin, Crack propagation and coalescence of brittle rock-like specimens with pre-existing cracks in compression, Eng. Geol. 187 (2015) 113–121.

[3] G.S. Esterhuizen, D.R. Dolinar, J.L. Ellenberger, Pillar strength in underground stone mines in the United States, Int. J. Rock Mech. Min. Sci. 48 (1) (2011) 42–50.

[4] P.O. Koons, P. Upton, A.D. Barker, The influence of mechanical properties on the link between tectonic and topographic evolution, Geomorphology 137 (1) (2012) 168–180.

[5] R.C. Liu, B. Li, L.Y. Yu, Y.J. Jiang, H.W. Jing, A discrete-fracture-network fault model revealing permeability and aperture evolutions of a fault after earthquakes, Int. J. Rock Mech. Min. Sci. 107 (7) (2018) 19–24.

[6] G. Papathanassiou, S. Valkaniotis, A. Ganas, N. Grendas, E. Kollia, The November 17th, 2015 Lefkada (Greece) strike-slip earthquake: field mapping of generated failures and assessment of macroseismic intensity ESI-07, Eng. Geol. 220 (2017) 13–30.

[7] I. Rigopoulos, B. Tsikouras, P. Pomonis, K. Hatzipanagiotou, Petrographic investigation of microcrack initiation in mafic ophiolitic rocks under uniaxial compression, Rock Mech. Rock Eng. 46 (5) (2013) 1061–1072.

[8] T. Kogure, H. Aoki, A. Maekado, T. Hirose, Y. Matsukura, Effect of the development of notches and tension cracks on instability of limestone coastal cliffs in the Ryukyus, Japan, Geomorphology 80 (3) (2006) 236–244.

[9] X. Li, S.J. Wang, T.Y. Liu, F.S. Ma, Engineering geology, ground surface movement and fissures induced by underground mining in the Jinchuan Nickel Mine, Eng. Geol. 76 (1–2) (2004) 93–107.

[10] R.C. Liu, B. Li, Y.J. Jiang, Critical hydraulic gradient for nonlinear flow through rock fracture networks: the roles of aperture, surface roughness, and number of intersections, Adv. Water Resour. 88 (2) (2016) 53–65.

[11] L. Causse, R. Cojean, J.A. Fleurisson, Interaction between tunnel and unstable slope-influence of time-dependent behavior of a tunnel excavation in a deep-seated gravitational slope deformation, Tunn. Undergr. Space Technol. 50 (2015) 270–281.

[12] M.M. Feng, J.Y. Wu, D. Ma, X.Y. Ni, B.Y. Yu, Z.Q. Chen, Experimental investigation on seepage property of saturated broken red sandstone of continuous gradation, Bull. Eng. Geol. Environ. (2017), https://doi.org/10.1007/s10064-017-1046-z.

[13] N. Koronakis, P. Kontothanassis, N. Kazilis, N. Gikas, Stabilization measures for shallow tunnels with ongoing translational movements due to slope instability, Tunn. Undergr. Space Technol. 19 (4–5) (2004) 495.

[14] R.C. Liu, B. Li, Y.J. Jiang, A fractal model based on a new governing equation of fluid flow in fractures for characterizing hydraulic properties of rock fracture networks, Comput. Geotech. 75 (5) (2016) 57–68.

[15] M. Makowska, D. Mège, F. Gueydan, J. Chéry, Mechanical conditions and modes of paraglacial deep-seated gravitational spreading in Valles Marineris, Mars, Geomorphology 268 (2016) 246–252.

[16] D. Boldini, A. Graziani, Remarks on axisymmetric modelling of deep tunnels in argillaceous formations-II: fissured argillites, Tunn. Undergr. Space Technol. 28 (3) (2012) 80–89.

[17] Y.C. Chiu, C.H. Lee, T.T. Wang, Lining crack evolution of an operational tunnel influenced by slope instability, Tunn. Undergr. Space Technol. 65 (2017) 167–178.

[18] L.C. Li, T.H. Yang, Z.Z. Liang, W.C. Zhu, C.A. Tang, Numerical investigation of groundwater outbursts near faults in underground coal mines, Int. J. Coal Geol. 85 (3–4) (2011) 276–288.

[19] R.C. Liu, Y.J. Jiang, B. Li, X.S. Wang, A fractal model for characterizing fluid flow in fractured rock masses based on randomly distributed rock fracture networks, Comput. Geotech. 65 (4) (2015) 45–55.
[20] M.G. Sweetenham, R.M. Maxwell, P.M. Santi, Assessing the timing and magnitude of precipitation-induced seepage into tunnels bored through fractured rock, Tunn. Undergr. Space Technol. 65 (2013) 62–75.
[21] T.H. Yang, J. Liu, W.C. Zhu, D. Elsworth, L.G. Tham, C.A. Tang, A coupled flow-stress-damage model for groundwater outbursts from an underlying aquifer into mining excavations, Int. J. Rock Mech. Min. Sci. 44 (1) (2007) 87–97.
[22] T.H. Yang, T. Xu, H.Y. Liu, C.A. Tang, B.M. Shi, Q.X. Yu, Stress-damage-flow coupling model and its application to pressure relief coal bed methane in deep coal seam, Int. J. Coal Geol. 86 (4) (2011) 357–366.
[23] T.H. Yang, W.C. Zhu, Q.L. Yu, H.L. Liu, The role of pore pressure during hydraulic fracturing and implications groundwater outbursts in mining and tunnelling, Hydrogeol. J. 19 (5) (2011) 995–1008.
[24] K. Zhang, T.H. Yang, H.B. Bai, R.P. Gamage, Longwall mining-induced damage and fractures: field measurements and simulation using FDM and DEM coupled method, Int. J. Geomech. 18 (1) (2018) 04017127.
[25] C. Wang, D.D. Tannant, P.A. Lilly, Numerical analysis of the stability of heavily jointed rock slopes using PFC2D, Int. J. Rock Mech. Min. Sci. 40 (3) (2003) 415–424.
[26] J.P. Latham, J. Xiang, M. Belayneh, H.M. Nick, C.F. Tsang, M.J. Blunt, Modelling stress-dependent permeability in fractured rock including effects of propagating and bending fractures, Int. J. Rock Mech. Min. Sci. 57 (1) (2012) 100–112.
[27] M.R. Ayatollahi, J. Akbardoost, Size and geometry effects on rock fracture toughness: Mode I fracture, Rock Mech. Rock Eng. 47 (2) (2014) 677–687.
[28] R.H. Cao, P. Cao, H. Lin, C.Z. Pu, K. Ou, Mechanical behavior of brittle rock-like specimens with pre-existing flaws under uniaxial loading: experimental studies and particle mechanics approach, Rock Mech. Rock Eng. 49 (3) (2016) 763–783.
[29] X.B. Li, T.S. Lok, J. Zhao, Dynamic characteristics of granite subjected to intermediate loading rate, Rock Mech. Rock Eng. 38 (1) (2005) 21–39.
[30] O. Mughieda, M.T. Omar, Stress analysis for rock mass failure with offset joints, Geotech. Geolog. Eng. 26 (5) (2008) 543–552.
[31] R.H.C. Wong, K.T. Chau, C.A. Tang, P. Lin, Analysis of crack coalescence in rock-like materials containing three flaws-Part I: experimental approach, Int. J. Rock Mech. Min. Sci. 38 (7) (2001) 909–924.
[32] J.Y. Wu, M.M. Feng, B.Y. Yu, G.S. Han, The length of pre-existing fissures effects on the mechanical properties of cracked red sandstone and strength design in engineering, Ultrasonics 82 (1) (2018) 188–199.
[33] S.Q. Yang, Crack coalescence behavior of brittle sandstone samples containing two coplanar fissures in the process of deformation failure, Eng. Fract. Mech. 78 (17) (2011) 3059–3081.
[34] S.Q. Yang, H.W. Jing, Strength failure and crack coalescence behavior of brittle sandstone samples containing a single fissure under uniaxial compression, Int. J. Fract. 168 (2) (2011) 227–250.
[35] X.P. Zhou, Y.T. Wang, Numerical simulation of crack propagation and coalescence in pre-fissured rock-like Brazilian disks using the non-ordinary state-based peridynamics, Int. J. Rock Mech. Min. Sci. 89 (10) (2016) 235–249.
[36] Y.H. Huang, S.Q. Yang, P.G. Ranjith, J. Zhao, Strength failure behavior and crack evolution mechanism of granite containing pre-existing non-coplanar holes: experimental study and particle flow modeling, Comput. Geotech. 88 (8) (2017) 182–198.
[37] J. Lee, Y.D. Ha, J.W. Hong, Crack coalescence morphology in rock-like material under compression, Int. J. Fract. 203 (1) (2017) 211–236.
[38] C.H. Park, A. Bobet, Crack coalescence in specimens with open and closed flaws: a comparison, Int. J. Rock Mech. Min. Sci. 46 (5) (2009) 819–829.
[39] C.H. Park, A. Bobet, Crack initiation, propagation and coalescence from frictional flaws in uniaxial compression, Eng. Fract. Mech. 77 (14) (2010) 2727–2748.
[40] M. Sagong, A. Bobet, Coalescence of multiple flaws in a rock-model material in uniaxial compression, Int. J. Rock Mech. Min. Sci. 39 (2) (2002) 229–241.
[41] C.A. Tang, P. Lin, R.H.C. Wong, K.T. Chau, Analysis of crack coalescence in rock-like materials containing three flaws-part II: numerical approach, Int. J. Rock Mech. Min. Sci. 38 (7) (2001) 925–939.
[42] R.H.C. Wong, K.T. Chau, Crack coalescence in a rock-like material containing two cracks, Int. J. Rock Mech. Min. Sci. 35 (2) (1998) 147–164.
[43] L.N.Y. Wong, H.H. Einstein, Systematic evaluation of cracking behavior in specimens containing single flaws under uniaxial compression, Int. J. Rock Mech. Min. Sci. 46 (3) (2009) 239–249.
[44] X.T. Feng, S. Chen, H. Zhou, Real-time computerized tomography (CT) experiments on sandstone damage evolution during triaxial compression with chemical corrosion, Int. J. Rock Mech. Min. Sci. 41 (2) (2004) 181–192.
[45] A. Ghazvinian, V. Sarfarazi, W. Schubert, M. Blumel, A study of the failure mechanism of planar non-persistent open joints using pfc2d, Rock Mech. Rock Eng. 45 (5) (2012) 677–693.
[46] A. Manouchehrian, M.F. Marji, Numerical analysis of confinement effect on crack propagation mechanism from a flaw in a pre-fissured rock under compression, Acta Mech. Sin. 28 (5) (2012) 1389–1397.
[47] A. Manouchehrian, M. Sharifzadeh, M.F. Marji, J. Gholamnejad, A bonded particle model for analysis of the flaw orientation effect on crack propagation mechanism in brittle materials under compression, Arch. Civ. Mech. Eng. 14 (1) (2013) 40–52.
[48] S.Q. Yang, Y.H. Huang, H.W. Jing, X.R. Liu, Discrete element modeling on fracture coalescence behavior of red sandstone containing two unparallel fissures under uniaxial compression, Eng. Geol. 178 (6) (2014) 28–48.
[49] X.P. Zhang, L.N.Y. Wong, Cracking processes in rock-like material containing a single flaw under uniaxial compression: a numerical study based on parallel bonded-particle model approach, Rock Mech. Rock Eng. 45 (5) (2012) 711–737.
[50] X.P. Zhang, L.N.Y. Wong, Crack initiation, propagation and coalescence in rock-like material containing two flaws: a numerical study based on bonded-particle model approach, Rock Mech. Rock Eng. 46 (5) (2013) 1001–1021.
[51] Z.N. Zhang, D.Y. Wang, H. Zheng, X.R. Ge, Interactions of 3D embedded parallel vertically inclined cracks subjected to uniaxial compression, Theor. Appl. Fract. Mech. 61 (1) (2012) 1–11.
[52] H. Lee, S. Jeon, An experimental and numerical study of fracture coalescence in pre-cracked specimens under uniaxial compression, Int. J. Solids Struct. 48 (6) (2011) 979–999.
[53] Z.Z. Liang, H. Xing, S.Y. Wang, D.J. Williams, C.A. Tang, A three-dimensional numerical investigation of the fracture of rock specimens containing a pre-existing surface flaw, Comput. Geotech. 45 (45) (2012) 19–33.
[54] X.T. Feng, W. Ding, Experimental study of limestone micro-fracturing under a coupled stress, fluid flow and changing chemical environment, Int. J. Rock Mech. Min. Sci. 44 (3) (2007) 437–448.
[55] X.T. Feng, W. Ding, D. Zhang, Multi-crack interaction in limestone subject to stress and flow of chemical solutions, Int. J. Rock Mech. Min. Sci. 46 (1) (2009) 159–171.
[56] C.A. Tang, S.Q. Kou, Crack propagation and coalescence in brittle materials under compression, Eng. Fract. Mech. 61 (3–4) (1998) 311–324.
[57] X.P. Zhang, L.N.Y. Wong, Loading rate effects on cracking behavior of flaw-contained specimens under uniaxial compression, Int. J. Fract. 180 (1) (2013) 93–110.
[58] S. Cao, W.D. Song, E. Yilmaz, Influence of structural factors on uniaxial compressive strength of cemented tailings backfill, Constr. Build. Mater. 174 (2018) 190–201.
[59] J.A.D.M. Franco, J.L. Armelin, J.A.F. Santiago, J.C.F. Telles, W.J. Mansur, Determination of the natural stress state in a Brazilian rock mass by back analysing excavation measurements: a case study, Int. J. Rock Mech. Min. Sci. 39 (8) (2002) 1005–1032.

[60] Y.H. Huang, S.Q. Yang, J. Zhao, Three-dimensional numerical simulation on triaxial failure mechanical behavior of rock-like specimen containing two unparallel fissures, Rock Mech. Rock Eng. 49 (12) (2016) 4711–4729.
[61] R.P. Tiwari, K.S. Rao, Physical modeling of a rock mass under a true triaxial stress state, Int. J. Rock Mech. Min. Sci. 41 (3) (2004) 396–401.
[62] Z.T. Bieniawski, Rock Mechanics Design in Mining and Tunneling, A.A. Balkema, Rotterdam, 1984.
[63] K. Hashiba, S. Okubo, K. Fukui, A new testing method for investigating the loading rate dependency of peak and residual rock strength, Int. J. Rock Mech. Min. Sci. 43 (6) (2006) 894–904.
[64] Y.P. Li, L.Z. Chen, Y.H. Wang, Experimental research on pre-cracked marble under compression, Int. J. Solids Struct. 42 (9–10) (2005) 2505–2516.
[65] X.B. Li, M. Tao, C.Q. Wu, K. Du, Q.H. Wu, Spalling strength of rock under different static pre-confining pressures, Int. J. Impact Eng. 99 (1) (2017) 69–74.
[66] S.K. Ray, M. Sarkar, T.N. Singh, Effect of cyclic loading and strain rate on the mechanical behaviour of sandstone, Int. J. Rock Mech. Min. Sci. 36 (4) (1999) 543–549.
[67] C.A. Tang, T. Xu, T.H. Yang, Z.Z. Liang, Numerical investigation of the mechanical behavior of rock under confining pressure and pore pressure, Int. J. Rock Mech. Min. Sci. 41 (3) (2004) 421–422.
[68] J.Y. Wu, M.M. Feng, B.Y. Yu, W.L. Zhang, X.Y. Ni, G.S. Han, Experimental investigation on dilatancy behavior of water-saturated sandstone, Int. J. Min. Sci. Technol. 28 (2) (2018) 323–329.
[69] R. Ulusay, The ISRM Suggested Methods for Rock Characterization, Testing and Monitoring: 2007–2014, Springer International Publishing, 2015.
[70] A. Bobet, H.H. Einstein, Fracture coalescence in rock-type materials under uniaxial and biaxial compression, Int. J. Rock Mech. Min. Sci. 35 (7) (1998) 863–888.
[71] S.Q. Yang, Y.Z. Jiang, W.Y. Xu, X.Q. Chen, Experimental investigation on strength and failure behavior of pre-cracked marble under conventional triaxial compression, Int. J. Solids Struct. 45 (17) (2008) 4796–4819.
[72] D. Huang, D.M. Gu, C. Yang, R.Q. Huang, G.Y. Fu, Investigation on mechanical behaviors of sandstone with two preexisting flaws under triaxial compression, Rock Mech. Rock Eng. 49 (2) (2016) 375–399.
[73] S.Q. Yang, Y.H. Dai, L.J. Han, Z.Q. Jin, Experimental study on mechanical behavior of brittle marble samples containing different flaws under uniaxial compression, Eng. Fract. Mech. 76 (12) (2009) 1833–1845.
[74] S. Cao, W.D. Song, Effect of filling interval time on the mechanical strength and ultrasonic properties of cemented coarse tailing backfill, Int. J. Miner. Process. 166 (2017) 62–68.
[75] S. Cao, E. Yilmaz, W.D. Song, Evaluation of viscosity, strength and microstructural properties of cemented tailings backfill, Minerals 8 (2018) 352.
[76] P.B. Zdeněk, S.P. Bai, R. Gettu, Fracture of rock: effect of loading rate, Eng. Fract. Mech. 45 (3) (1993) 393–398.
[77] M. Cai, P.K. Kaiser, Y. Tasaka, T. Maejimac, H. Moriokac, M. Minami, Generalized crack initiation and crack damage stress thresholds of brittle rock masses near underground excavations, Int. J. Rock Mech. Min. Sci. 41 (5) (2004) 833–847.
[78] S.C. Cowin, Constitutive relations that imply a generalized Mohr–Coulomb criterion, Acta Mech. 20 (1–2) (1974) 41–46.
[79] E. Hoek, Estimating Mohr–Coulomb friction and cohesion values from the Hoek–Brown failure criterion, Int. J. Rock Mech. Min. Sci. Geomech. Abstr. 27 (3) (1990) 227–229.
[80] E. Hoek, P.K. Kaiser, W.F. Bawden, Support of Underground Excavations in Hard Rock, Balkema, Rotterdam, The Netherlands, 1995.
[81] Y. Obara, Y. Ishiguro, Measurements of induced stress and strength in the near-field around a tunnel and associated estimation of the Mohr–Coulomb parameters for rock mass strength, Int. J. Rock Mech. Min. Sci. 41 (5) (2004) 761–769.
[82] T. Benz, R. Schwab, A quantitative comparison of six rock failure criteria, Int. J. Rock Mech. Min. 45 (7) (2008) 1176–1186.
[83] M.Q. You, True-triaxial strength criteria for rock, Int. J. Rock Mech. Min. Sci. 46 (1) (2009) 115–127.
[84] M.Q. You, Comparison of the accuracy of some conventional triaxial strength criteria for intact rock, Int. J. Rock Mech. Min. Sci. 48 (5) (2011) 852–863.
[85] M.Q. You, Mechanical characteristics of the exponential strength criterion under conventional triaxial stresses, Int. J. Rock Mech. Min. Sci. 47 (2) (2010) 195–204.
[86] Y.H. Huang, S.Q. Yang, M.R. Hall, W.L. Tian, P.F. Yin, Experimental study on uniaxial mechanical properties and crack propagation in sandstone containing a single oval cavity, Arch. Civ. Mech. Eng. 18 (4) (2018) 1359–1373.
[87] D. Martin, N.A. Chandler, The progressive fracture of Lac du Bonnet Granite, Int. J. Rock Mech. Min. Sci. Geomech. Abstr. 31 (6) (1994) 643–659.